*J. Fluid Mech.* (2001), *vol.* 426, *pp.* 297–326. Printed in the United Kingdom



# Turbulent flow between a rotating and a stationary disk

By MAGNE LYGREN AND HELGE I. ANDERSSON

Division of Applied Mechanics, Norwegian University of Science and Technology, N-7491 Trondheim, Norway

(Received 14 February 2000 and in revised form 7 August 2000)

Turbulent flow between a rotating and a stationary disk is studied. Besides its fundamental importance as a three-dimensional prototype flow, such flow fields are frequently encountered in rotor–stator configurations in turbomachinery applications. A direct numerical simulation is therefore performed by integrating the time-dependent Navier–Stokes equations until a statistically steady state is reached and with the aim of providing both long-time statistics and an exposition of coherent structures obtained by conditional sampling. The simulated flow has local Reynolds number $r^2\omega/\nu = 4 \times 10^5$ and local gap ratio $s/r = 0.02$, where $\omega$ is the angular velocity of the rotating disk, $r$ the radial distance from the axis of rotation, $\nu$ the kinematic viscosity of the fluid, and $s$ the gap width.

The three components of the mean velocity vector and the six independent Reynolds stresses are compared with experimental measurements in a rotor–stator flow configuration. In the numerically generated flow field, the structural parameter $a_1$ (i.e. the ratio of the magnitude of the shear stress vector to twice the mean turbulent kinetic energy) is lower near the two disks than in two-dimensional boundary layers. This characteristic feature is typical for three-dimensional boundary layers, and so are the misalignment between the shear stress vector and the mean velocity gradient vector, although the degree of misalignment turns out to be smaller in the present flow than in unsteady three-dimensional boundary layer flow. It is also observed that the wall friction at the rotating disk is substantially higher than at the stationary disk.

Coherent structures near the disks are identified by means of the $\lambda_2$ vortex criterion in order to provide sufficient information to resolve a controversy regarding the roles played by sweeps and ejections in shear stress production. An ensemble average of the detected structures reveals that the coherent structures in the rotor–stator flow are similar to the ones found in two-dimensional flows. It is shown, however, that the three-dimensionality of the mean flow reduces the inter-vortical alignment and the tendency of structures of opposite sense of rotation to overlap. The coherent structures near the disks generate weaker sweeps (i.e. quadrant 4 events) than structures in conventional two-dimensional boundary layers. This reduction in the quadrant 4 contribution from the coherent structures is believed to explain the reduced efficiency of the mean flow in producing Reynolds shear stress.

## 1. Introduction

The flow between a rotating and a fixed parallel disk has received much attention due to its relevance to applications in turbomachinery, where the two-disk flow serves as a model problem for rotor–stator flows. This flow is also known to be one of very

few examples of three-dimensional flows that in the laminar case are described by exact solutions to the Navier–Stokes equations. Three-dimensional boundary layers are commonly found in engineering flows, making determining and understanding the behaviour of these boundary layers important. The flow between rotating disks is one of the simplest cases where the boundary layers are three-dimensional and this flow is therefore well suited for studying the effects of mean-flow three-dimensionality on the turbulence and its structures.

### 1.1. *Rotor–stator flows*

Daily & Nece (1960) studied experimentally an enclosed rotor–stator flow and identified four flow regimes: two laminar and two turbulent, each having either merged or separated boundary layers. (Here and in the following the term 'separated' boundary layers means that the boundary layers near the two disks are separated from each other by an inviscid rotating core.) The different regimes were found to depend on the rotational Reynolds number $Re_R = R^2\omega/\nu$ and the gap ratio $G_R = s/R$, where $R$ is the radius of the disks, $\omega$ the angular frequency of the rotating disk, $\nu$ the kinematic viscosity and $s$ the axial distance between the disks.

The laminar flow between unshrouded disks is described by similarity equations originating from the von Kármán similarity principle. Von Kármán (1921) considered an infinite disk rotating in an unbounded viscous fluid and reduced the Navier–Stokes equations to a pair of nonlinear ordinary differential equations by using a similarity principle. Batchelor (1951) generalized the original one-disk problem to include a second parallel disk and argued qualitatively that for the case with only one disk rotating, boundary layers would form at both disks and in the core the fluid would rotate. In contrast, Stewartson (1953) claimed that there would only be a boundary layer near the rotating disk, and the fluid in the core would not rotate. The controversy between Batchelor and Stewartson has triggered many investigations on this flow, ranging from rigorous mathematical analysis to numerical solutions and experiments. Zandbergen & Dijkstra (1987) provide a review on these investigations showing that the similarity equations do not generally have unique solutions. The two qualitatively different solutions advocated by Batchelor and Stewartson can thus both be found from the similarity equations. For laminar flow between finite disks, Brady & Durlofsky (1987) have shown that closed-end flows resemble the Batchelor solution, while open-end flows resemble the Stewartson solution.

In real situations the flow between large disks will undergo a transition to turbulence when the local Reynolds number $Re_r = r^2\omega/\nu$, based on the radial coordinate $r$, is sufficiently large. Cooper & Reshotko (1975) pointed out that near the axis of rotation the flow is laminar and the boundary layer thickness is approximately constant. If the gap width is large the boundary layers are separated. After transition to turbulence the separated boundary layers thicken and eventually merge when the local gap ratio $G_r = s/r$ is sufficiently small. The accurate radial position of transition depends both on $Re_r$ and the distance between the disks. For one disk rotating in a quiescent environment the flow is fully turbulent at a local rotational Reynolds number $Re_r = 3.9 \times 10^5$, according to Kobayashi (1994). For the confined rotor–stator configurations the transition occurs at lower Reynolds numbers. Owen & Rogers (1989) concluded, based on the experimental data by Daily & Nece (1960), that the transition was completed at $Re_r \approx 1.5 \times 10^5$ for gap ratios $G_r$ larger than 0.04. For smaller gap ratios ($G_r \lesssim 0.04$) the transition to turbulence takes place at lower Reynolds numbers. In an experiment with separated boundary layers ($G_R = 0.08$), Itoh *et al.* (1992) found that the rotor-side boundary layer was laminar for $Re_r = 1.6 \times 10^5$,

turbulent for $Re_r = 3.6 \times 10^5$ and fully turbulent for $Re_r = 4.6 \times 10^5$. The boundary layer near the stator was found to be turbulent at lower local Reynolds numbers. Between more closely spaced disks the transition takes place at lower $Re_r$, as can be seen in Itoh (1995). Cheah *et al.* (1994) also found that near the stationary disk the boundary layer was turbulent at lower Reynolds numbers than the boundary layer near the rotating disk. The differences in the transition Reynolds numbers near the two disks were explained by Itoh *et al.* (1992) as a consequence of the flow being decelerated near the stator and accelerated near the rotor. Cheah *et al.* (1994) argued that near the rotor the transition is delayed since the fluid arrives from the laminar region near the axis of rotation, while the flow near the stator arrives from a turbulent region further out from the axis and therefore remains turbulent at smaller radii.

### 1.2. *Three-dimensional turbulent boundary layers*

A three-dimensional turbulent boundary layer (3DTBL) is a boundary layer where the mean velocity vector changes direction with the distance from the wall, while the direction of the mean velocity in a two-dimensional turbulent boundary (2DTBL) remains constant. 3DTBLs are commonly found in engineering applications such as over swept wings, in curved ducts and in rotating machinery. Although the turbulence statistics and structures are similar for a 3D- and 2DTBL, there are some important differences. The Reynolds shear stress vector is the vector in the plane parallel to the wall with components $-\overline{u'v'}$ and $-\overline{w'v'}$, expressed in a coordinate system with $y$ being the wall-normal direction and $v$ the corresponding velocity component. In a two-dimensional boundary layer the shear stress vector is aligned with the velocity gradient vector with components $\partial U/\partial y$ and $\partial W/\partial y$. In a 3DTBL, on the other hand, this is not generally the case (Bradshaw & Pontikos 1985). Especially in non-equilibrium 3DTBLs the stress–strain lag angle can be large (e.g. Bradshaw & Pontikos 1985; Moin *et al.* 1990) resulting in poor performance of turbulence models based on the isotropic eddy-viscosity hypothesis. Another noticeable change caused by the three-dimensionality of the mean flow is that the magnitude $\tau$ of the shear stress vector relative to the turbulent kinetic energy $k$ is reduced. This ratio is commonly expressed through the structural parameter $a_1 = \tau/2k$. The reduction in $a_1$ is an indication that the turbulence is less efficient in extracting energy from the mean flow than in a 2DTBL. For most cases considered in the review by Johnston & Flack (1996), $a_1$ was found to be reduced below the generally accepted value 0.15 for conventional 2DTBLs. The so-called 'Trondheim Trials' (Fanneløp & Krogstad 1975) showed that these changes in turbulence structure influence the performance of turbulence models applied to 3DTBLs. Most experimental studies on 3DTBLs have additional complicating effects such as streamwise pressure gradients, wall curvature or system rotation. Spalart & Watmuff (1993) and Coleman, Kim & Spalart (2000), e.g., showed that an adverse pressure gradient also reduced the level of $a_1$. It can therefore be difficult to distinguish between the three-dimensionality of the mean flow and these complicating effects when discussing the reasons for the observed changes in the turbulence. 3DTBLs have been simulated numerically by Spalart (1989), Moin *et al.* (1990), Sendstad & Moin (1991), Coleman, Ferziger & Spalart (1990), Coleman, Kim & Spalart (1996), Coleman *et al.* (2000), Le, Coleman & Kim (1999) and Wu & Squires (1999).

The effect of the mean-flow three-dimensionality on the turbulent Reynolds stresses has motivated research on quasi-coherent structures in the near-wall region. It is believed that the three-dimensionality modifies the coherent vorticity structures found in the two-dimensional boundary layers. The coherent structures in the near-wall

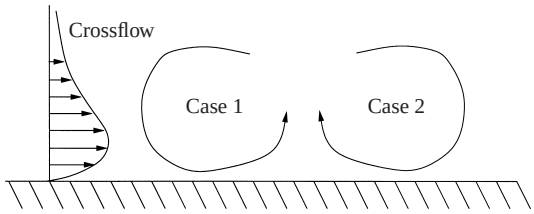


FIGURE 1. Streamwise vortex labels as defined by Shizawa & Eaton (1992).

regions of 2DTBLs consist of, as described by Robinson (1991), streamwise streaks of high- and low-speed fluid together with quasi-streamwise vortices. Jeong *et al.* (1997) further refined the picture of the coherent structures in the region $y^+ \leqslant 60$ by directly extracting the vortical structures by means of the vortex definition proposed by Jeong & Hussain (1995). Their coherent structures were elongated quasi-streamwise vortices inclined in the vertical plane and tilted in the horizontal plane. The mutual interaction of the vortices produced long regions of high- and low-speed streaks. These vortices were responsible for most of the turbulence production.

Investigations on structural changes caused by the three-dimensionality have focused on the strength and symmetry of the vortices of opposite sign, as shown in the review by Eaton (1995) on experimental studies of coherent structures in 3DTBLs. In the following, the nomenclature by Shizawa & Eaton (1992) is adopted to label the vortices of opposite sign. A Case 1 vortex has induced near-wall velocity in the direction of the crossflow (see figure 1), while Case 2 has oppositely directed velocity near the wall. Bradshaw & Pontikos (1985), who measured the turbulence on a swept wing, argued that the reduction in $a_1$ is caused by the spanwise shear that tilts the large eddies (initially developed in a 2DTBL) sideways and, hence, reduces their efficiency in producing shear stress. Anderson & Eaton (1989) studied the skewed boundary layer caused by an upstream-facing wedge. They suggested that the observed stabilization of the turbulence may be caused by a reduction in the number of localized vortices having the opposite sign of vorticity to that of the streamwise vorticity associated with the mean flow.

Shizawa & Eaton (1992) used a vortex generator to embed a vortex in the boundary layer approaching a wedge. The generated vortices were substantially greater than the naturally occurring vortices found in turbulent boundary layers. The vortices decayed faster in the three-dimensional boundary layer than in an equivalent two-dimensional flow. In addition, Case 1 vortices produced weak ejections while the ejections from Case 2 vortices were very strong. In contrast, in a study of the boundary layer over a rotating disk in a quiescent fluid, Littell & Eaton (1994) concluded that Case 1 vortices produced strong ejections and weak sweeps while Case 2 generated stronger sweeps than ejections. The number of vortices of opposite sign were approximately equal. Their conclusions were based on two-point conditional correlations that were asymmetric in the spanwise direction, an asymmetry that is not possible in a 2DTBL. Chiang & Eaton (1996) used hydrogen bubble visualization to study the structures in the flow over a rotating disk. They refined the findings of Littell & Eaton (1994) and concluded that Case 1 and Case 2 vortices were equally likely to produce ejections, but the ejections caused by Case 1 were stronger than the Case 2 ejections. From another experiment on the rotating disk Kang, Choi & Yoo (1998) concluded that the asymmetry in the conditional averages of Littell & Eaton (1994) were not caused by Reynolds-stress-producing events and the vortical structures were near symmetric

in the spanwise direction. Flack (1997), in the flow in a curved bend, also found contrary results to Littell & Eaton (1994). Stress-producing events near the vortices in the bend were not influenced by the sign of rotation of the vortices. Sendstad & Moin (1991) studied the fluid particle trajectories near vortices in a two-dimensional boundary layer which suddenly experiences a spanwise pressure gradient. In general they supported the conclusions of Littell & Eaton (1994). In a recent simulation of two-dimensional flow where the wall is suddenly set in motion, Le *et al.* (1999) also found that the imposed three-dimensionality led to asymmetry between the vortices of opposite sign.

It is possible that some of the discrepancies observed in these structural studies can be explained by differences in the origin of the three-dimensionality. Structures in an originally two-dimensional boundary layer which experiences a sudden crossflow may be different from the structures in a boundary layer which is three-dimensional from its laminar origin, i.e. like on the rotating disk. The discrepancies also make it evident that further investigations are needed in order to shed more light on flow phenomena associated with 3DTBLs and, in particular, to settle the prevailing controversy regarding the role played by the near-wall vortical structures.

In this paper we report on a direct numerical simulation performed to study the turbulent flow between 'infinite' rotating and stationary disks. The main motivation for our investigation is to explore the modification of the turbulence due to the three-dimensionality of the mean flow. In order to enhance the physical understanding of how and why the turbulence is affected, not are only conventional turbulence statistics needed, but also ensemble averages of coherent flow structures become of crucial importance. First, however, the numerical simulation code, boundary condition treatment as well as choice of parameters for the simulation are described in § 2. Comparisons between long-time statistics from the simulation and experimental data from a laboratory study by Itoh (1995) are made in § 3. Since turbulent plane Couette flow may be considered as the two-dimensional analogue of the rotating disk flow, statistical data are also compared with results from a simulation by Bech *et al.* (1995). In § 4 the focus is on the coherent flow structures, and finally some conclusions and closing remarks are provided in § 5.

## 2. Simulation overview

A direct numerical simulation (DNS) is performed to complement the experimental studies of flows between a rotating and a stationary disk. As far as the authors are aware, direct simulations of fully turbulent rotor–stator flows have not been performed before.

The flow of an incompressible Newtonian fluid between two infinite parallel disks separated by a distance $s$ (see figure 2) is considered. One disk is stationary, i.e. non-rotating, while the other disk is rotating with constant angular frequency $\omega$. At a given radial position $r$ the flow is governed by the four independent parameters $r$, $s$, $\omega$ and $\nu$ which can be combined in different ways into two non-dimensional numbers. Here, the local rotational Reynolds number $Re_r = r^2\omega/\nu$ and the local gap ratio $G_r = s/r$ are adopted as independent dimensionless parameters.

### 2.1. *Numerical approach*

The Navier–Stokes equations are expressed in cylindrical coordinates $(r, \theta, z)$ and solved on the computational domain represented by solid lines in figure 2. We consider the angular section $\Delta\theta$ between the two radial coordinate surfaces $r_1$ and $r_2$.

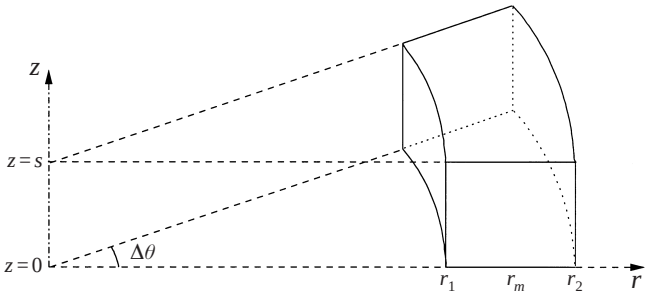


FIGURE 2. Sketch of computational domain and coordinate system.

The rotating disk (rotor) is at $z = 0$ while the stationary disk (stator) is at $z = s$; $r_m = (r_1 + r_2)/2$ is the radial coordinate in the centre of the computational domain.

The governing equations are discretized using a second-order finite-difference scheme in cylindrical coordinates. The Poisson equation for pressure is solved by a multigrid method, see Andersson, Lygren & Kristoffersen (1998) for details. The flow field is advanced in time by using a fractional-step method and a second-order Adams–Bashforth time discretization scheme.

In the tangential direction conventional periodic boundary conditions are applied and at the disks no-slip conditions are imposed. Since the flow is statistically evolving in the radial direction, full periodicity cannot be used at the coordinate surfaces $r_1$ and $r_2$. We are interested in the fully turbulent flow between the disks and a low gap ratio. Littell & Eaton (1994), for a single disk, and Itoh *et al.* (1992), Cheah *et al.* (1994) and Itoh (1995), for the two-disk problem, have noticed that the turbulence statistics vary relatively slowly in the radial direction, except near transition. This slow variation of the turbulence statistics suggests that quasi-periodic boundary conditions can be applied between the coordinate surfaces $r_1$ and $r_2$. The boundary condition treatment adopted in the present study is almost identical to that used in the large-eddy simulations of the flow over a rotating disk by Wu & Squires (1999, 2000). Their method for generating time-dependent boundary conditions is based on the scheme Lund, Wu & Squires (1998) have developed for simulating spatially developing boundary layers. In contrast to the approach by Spalart (1988) in his simulations of two-dimensional spatially developing boundary layers, the boundary treatment by Lund *et al.* (1998) does not involve any coordinate transformation. The flow field at a downstream location is rescaled and recycled at the inlet. The scheme of Lund *et al.* (1998) was simplified by Wu & Squires (2000) when simulating the flow over a rotating disk. For the rotor–stator flow the only essential modification of the boundary treatment for one disk is how the global mass conservation is obtained. The specific steps used in this study are:

1. At the beginning of the time step $t + \Delta t$ the velocity fields are decomposed into a mean and fluctuating part,

$$u_i(r, \theta, z, t) = U_i(r, z) + u_{i,rms}(r, z)u_{i,P}(r, \theta, z, t), \quad i = r, \theta, z, \tag{2.1}$$

where $U_i$ denotes the mean velocity components, $u_{i,rms}$ is the root-mean-square of the turbulence fluctuations and $u_{i,P}$ the fluctuating signal with root-mean-square value equal to one; $u_{i,P}$ is assumed periodic between $r_1$ and $r_2$. The mean values are averaged in the tangential direction and in time.

2. Quasi-periodicity is imposed by using $u_{i,P}(r, \theta, z, t)$ to generate the velocities at $r_1$

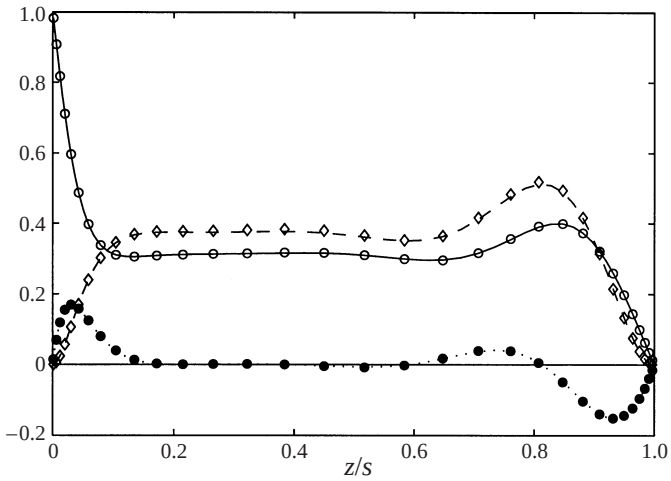


FIGURE 3. Velocity profiles from a simulation (lines) and the Batchelor solution of the von Kármán similarity equations (symbols); laminar flow at $Re_s = 900$. Rotating disk at $z = 0$. ———, ○, $U_\theta/r\omega$; · · · · · ·, •, $U_r/r\omega$; — — —, ◇, $-U_z/(\nu\omega)^{1/2}$.

and $r_2$ in the following way:

$$u_i(r_1, \theta, z, t + \Delta t) = U_i(r_1, z) + u_{i,rms}(r_1, z)u_{i,P}(r \to r_2, \theta, z, t), \tag{2.2}$$

$$u_i(r_2, \theta, z, t + \Delta t) = U_i(r_2, z) + u_{i,rms}(r_2, z)u_{i,P}(r_1 \leftarrow r, \theta, z, t). \tag{2.3}$$

Here $r_1 \leftarrow r$ and $r \to r_2$ represent radial positions adjacent to the two planes $r_1$ and $r_2$, respectively.

3. Two different methods for specifying $U_i$ and $u_{i,rms}$ at $r_1$ and $r_2$ have been tested. First, $U_i$ and $u_{i,rms}$ at $r_1$ and $r_2$ were obtained by linear extrapolation of $U_i$ and $u_{i,rms}$ at the radial plane $r = r_m$ assuming that $U_\theta$, $U_r$ and r.m.s. values are proportional to $r$, while $U_z$ is independent of $r$. Second, $U_i$ and $u_{i,rms}$ at $r_1$ and $r_2$ were calculated by a linear approximation $a_0 + a_1 r$, where $a_0$ and $a_1$ were computed in the least-squares sense from the interior points of $U_i$ and $u_{i,rms}$. Statistics from the two methods did not differ significantly. The first method was adopted in the present study.

4. Global mass conservation is obtained by enforcing the radial velocity component $u_r$ to have zero net flux through $r_1$ and $r_2$ at every time step.

The assumptions made in step 3 are supported by experimental findings (e.g. Itoh 1995), but are not necessarily exact. As pointed out by Wu & Squires (2000), the boundary treatment represents an approximation of the physical problem and may be regarded as necessary to achieve a feasible computational problem. Since $U_i(r, z)$ and $u_{i,rms}(r, z)$ are initially unknown, the time-averaging of mean and r.m.s. values used in the boundary treatment is performed with a weight which decreases exponentially backwards in time.

As a first test of the boundary condition treatment, we calculated the laminar flow using different gap ratios and rotational Reynolds numbers. The size of the computational domain was then $3s \times 10s \times s$ in the radial, tangential and wall-normal directions. The grid sizes were up to $32 \times 32 \times 64$ in the corresponding directions. Initially, the wall-normal and radial velocities were zero and the tangential velocity varied linearly from the rotating to the stationary disk. All the different test cases were in very good agreement with the Batchelor solutions of the von Kármán similarity

| | $u_{\theta\tau}s/\nu$ | $u_{r\tau}s/\nu$ | $u_\tau s/\nu$ |
|---|---|---|---|
| Rotor side | 265.7 | 182.1 | 279.3 |
| Stator side | 213.5 | 125.9 | 219.7 |

TABLE 1. Reynolds numbers based on wall friction velocities at the rotating and the stationary disk. Tangential friction velocity $u_{\theta\tau} = (\nu\partial U_\theta/\partial z)^{1/2}$, radial friction velocity $u_{r\tau} = (\nu\partial U_r/\partial z)^{1/2}$, total friction velocity $u_\tau = (u_{\theta\tau}^4 + u_{r\tau}^4)^{1/4}$.

equations obtained by using a multiple shooting technique. It is noteworthy that the solution of the similarity equations depends solely on the gap Reynolds number $Re_s = s^2\omega/\nu$. Figure 3 shows that the numerical simulation faithfully reproduces the rather complicated velocity profiles in the laminar flow at $Re_{r_m} = r_m^2\omega/\nu = 10^3$ and $Re_s = 900$.

### 2.2. *Simulation parameters*

The direct numerical simulation of the turbulent rotor–stator flow is performed with a rotational Reynolds number $Re_{r_m} = 4 \times 10^5$ and gap ratio $G_{r_m} = 0.02$. It is possible to increase $Re_{r_m}$ and decrease the gap ratio and still satisfy the resolution requirements for a DNS of turbulent flows. However, different test simulations showed that by lowering the gap ratio the size of the radial velocity component decreases, thereby reducing the mean-flow three-dimensionality. In fact, in the limit $g \to 0$ the three-dimensional flow between the two disks approaches the plane two-dimensional Couette flow. Since the primary goal of this study is to investigate three-dimensional effects, the particular parameter combination $Re_{r_m} = 4 \times 10^5$ and $G_{r_m} = 0.02$ is considered. As far as we know, the laboratory experiment with parameters closest to these was that performed recently by Itoh (1995). He measured both mean velocities and all the components of the full Reynolds stress tensor in the gap between a rotating disk and a cylindrical casing.

The size of the computational domain is $3.5s \times 7s \times s$ in the radial, tangential and axial directions and the corresponding numbers of grid points are $192 \times 192 \times 128$. The friction on the rotating disk is generally higher than on the stationary disk. The reason is that there is a net flow of angular momentum out of the computational domain. Individual Reynolds numbers based on the friction velocity at the rotating disk and at the stationary disk can therefore be defined, as listed in table 1. Note that these Reynolds numbers are based on the whole distance $s$ between the disks, in contrast to common practice for plane channel flows where it is customary to use half the distance between the plates. The size of the smallest computational cells was $r_m\Delta\theta^+ \times \Delta r^+ \times \Delta z^+_{min} \approx 10 \times 5 \times 0.4$ in rotor-side wall units and $8 \times 4 \times 0.3$ in stator-side wall units. In the wall-normal direction the grid is stretched and the maximal $\Delta z^+$ is approximately 4 based on the rotor-side friction velocity.

The initial velocity fields were the laminar-flow (Batchelor) velocity profiles with random disturbances superimposed. After the time-dependent flow had settled at a statistically steady state, turbulence statistics were gathered during 2.9 global time units (i.e. in terms of $\omega^{-1}$) and 1300 and 850 inner time units $t_* = \nu/u_{\theta\tau}^2$ where the friction velocity is at the rotating and stationary disk, respectively.

Two-point correlation coefficients for the three velocity components near the disks are given in figure 4. The correlations are small at large separations, indicating that the circumferential extent of the computational domain is sufficiently large. The

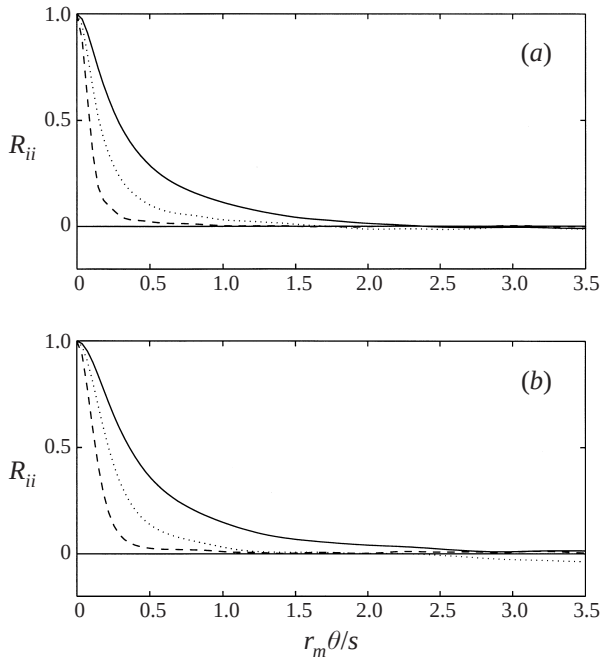


FIGURE 4. Two-point correlation coefficients near the rotating (*a*) and stationary (*b*) disks. Relative distance to the disks is 5 wall units. ———, $R_{\theta\theta}$; · · · · · ·, $R_{rr}$; — — —, $R_{zz}$.

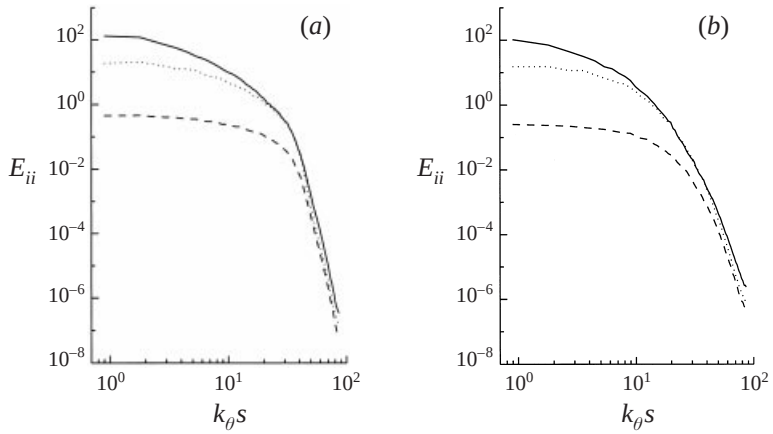


FIGURE 5. One-dimensional energy spectra near the rotating (*a*) and stationary (*b*) disks. Relative distance to the disks is 5 wall units. ———, $E_{\theta\theta}$; · · · · · ·, $E_{rr}$; — — —, $E_{zz}$.

correlations decay more slowly to zero at the stator side than at the rotor side since coherent structures like high- and low-speed streaks scale on wall units and $Re_\tau = u_\tau s/\nu$ is smaller near the stator, cf. table 1. The corresponding streamwise energy spectra are shown in figure 5. The energy associated with highest wavenumbers is at least five decades lower than the energy content of low-wavenumber motions.

## 3. Mean field and turbulence statistics

The statistical data presented in this section are averaged in both time and in the homogeneous tangential direction. In addition the data have also been averaged in the radial direction after first being normalized with either the local disc velocity or the local friction velocity. After this normalization the resulting turbulence statistics vary only marginally with the radial position $r$, thereby justifying the subsequent averaging also in the radial direction.

Some of the results are compared with experimental data by Itoh (1995) who considered a pair of enclosed disks, one of which was rotating. The clearance between the disks was only 4 mm, thus making the gap ratio small. Hot-wire measurements of the full Reynolds-stress tensor were reported for a local rotational Reynolds number $Re_r = 4.6 \times 10^5$. The local gap ratio was $G_r = 0.02$, and the measurements were taken at a radial position $r = 0.8R$ where $R$ is the radius of the disks.

It is also of interest to compare some results from the flow between the two disks with the two-dimensional counterpart of the rotor–stator flow in order to study effects of the three-dimensionality on the turbulence. Some of the present statistics are therefore compared with DNS data of the plane Couette flow by Bech *et al.* (1995). The Reynolds number of that flow, based on half the velocity difference and the half-distance $h$ between the moving planes, was 1300, whereas the wall-friction Reynolds number was 164.4 (based on $2h$ and thus comparable with those in table 1).

### 3.1. *Mean field*

The profiles of the mean velocities in figure 6($a$) show that the tangential velocity profile is similar to the profile of streamwise velocity in turbulent plane Couette flow. Whereas the velocity at the channel centre is half the wall velocity in the Couette flow due to symmetry reasons, the angular frequency of the fluid at $z = s/2$ is $0.432\omega$ in the present simulation. Since the mean axial component $U_z$ is negative in the gap between the disks, and since the tangential velocity is decreasing with the distance from the rotor, there is a net outflow of angular momentum from the computational domain, as mentioned in the previous section. To balance this angular momentum outflow the gradient of the tangential mean velocity is higher near the rotor than at the stator, thus giving rise to a higher frictional torque at the rotor. The tangential core velocity is therefore below $\omega r/2$. By assuming an inviscid core rotating with a constant angular velocity between infinite disks and 1/7-power-law mean velocity profiles in the boundary layers, Owen & Rogers (1989) found using two different approaches that the velocity of the core would be $0.426\omega r$ or $0.431\omega r$, which is surprisingly close to the $0.432\omega r$ found between the disks in the present study. The tangential mean velocity in the DNS is in good agreement with the experimental data from Itoh (1995), especially near the rotating disk. At $z = s/2$ the tangential velocity is approximately $0.45\omega r$ in his experiment. In addition to the fact that Itoh (1995) considered finite disks, some differences in the mean velocity profiles can be a Reynolds-number effect.

The radial crossflow in figure 6($a$) varies continuously across the gap, in contrast to rotor–stator flows with large clearances. The crossing $U_r = 0$ is at $z/s = 0.469$. The radial component agrees well with Itoh (1995). The axial mean velocity is everywhere small and negative.

Scaled in wall units the streamwise mean velocities relative to the disks in figure 6($b$) follow rather closely the law of the wall. The normalization is based on the tangential friction velocity $u_{\theta\tau}$ and $z^+_{rel}$ is the relative distance to the nearest disk. In the same plot, the radial mean velocities are also presented where $-U_r$ is shown near

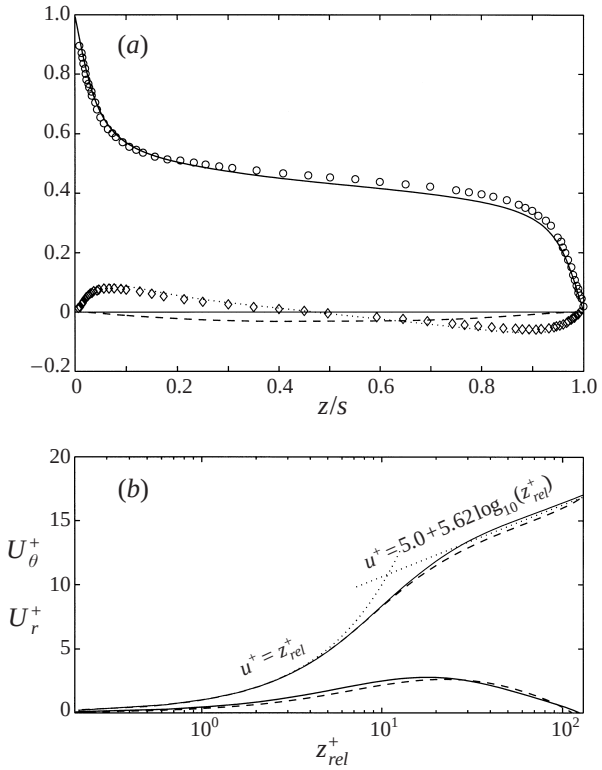


FIGURE 6. (*a*) Mean velocities in global coordinates. Symbols are from Itoh (1995). ——, ○, $U_\theta/r\omega$; · · · · · ·, ◇, $U_r/r\omega$; — — —, $U_z/r\omega$. (*b*) Mean tangential and radial velocities in wall units near the rotor (solid) and the stator (dashed). Normalized with tangential friction velocity.

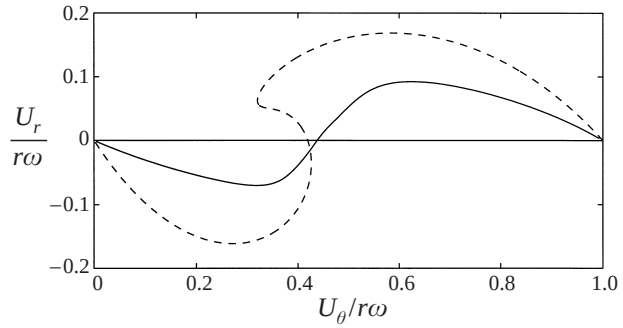


FIGURE 7. Polar plot of $U_\theta$ and $U_r$ in the whole gap between the disks from the present simulation (solid) and the laminar von Kármán solution (dashed). Note that the boundary layer near the rotating disk is to the right in this plot.

the stator side. The maximum crossflow is at $z^+_{rel} = 15$ near the rotor and $z^+_{rel} = 22$ near the stator. Several authors (e.g. Itoh *et al.* 1992; Littell & Eaton 1994; Wu & Squires 1997) have found that the peak in the crossflow in a 3DTBL does not scale in inner variables. In wall units the location of the peak is typically further out from the wall when the Reynolds number is larger.

A polar plot of the tangential and radial velocity components is shown in figure 7. The laminar solution obtained from the von Kármán similarity equations (Batchelor

solution) is included in this plot. The turbulent flow differs significantly from the laminar flow. In the turbulent case, the boundary layers near the rotor and stator both exhibit the characteristic triangular form found in 3DTBLs. This polar plot moreover indicates that the three-dimensionality is strongest near the rotor. However, to compare the amount of three-dimensionality in the two boundary layers, it is more appropriate to relate the crossflow to the tangential 'free-stream' velocity relative to the respective disks. The relative velocity for the rotating disk at $z = s/2$ is $U_{\theta,rel} = \omega r - 0.432\omega r = 0.568\omega r$ and for the stationary disk $U_{\theta,rel} = 0.432\omega r$. The peak of the crossflow distribution turns out to be approximately 16% of $U_{\theta,rel}$ near both disks, thus indicating that the strength of the three-dimensionality is almost the same in the rotor and stator boundary layers. In the 3DTBL with rotating free-stream velocity (Spalart 1989) and in the turbulent Ekman layer (Coleman *et al.* 1990), the peak value of the crossflow was about 22% of the free-stream velocity. In rotating disk flow, the crossflow was about 11% of the local disk velocity (Littell & Eaton 1994).

### 3.2. *Turbulence field*

All six Reynolds stresses are given in figure 8. They are normalized with the wall friction velocity $u_\tau$ (see table 1). The data from Itoh (1995) are included in the same plots. The general trend is that the experimental and numerical data fit quite well for the boundary layer near the stationary disk. Near the rotating disk the experimental values are generally lower than the simulated ones.†

One reason for the discrepancies could simply be that the flow between infinite disks is considered in the DNS, while Itoh (1995) studied a case with shrouded disks. When the stresses are not normalized the turbulence intensity is higher near the rotor than the stator in the simulation. In the experiment this dimensional intensity is almost the same near the two disks. This can be a consequence of increased mixing between the boundary layers due to the presence of the fixed outer shroud. Near the rotating disk the radial crossflow transports fluid outwards from smaller radii where the flow is laminar. It is possible that this could lead to lower turbulence intensities. The boundary condition treatment described in § 2.1 would not capture this effect. Finally, the differences between the experiment and DNS could partly be ascribed to the difference in Reynolds numbers.

The tangential turbulent intensity has a distinct maximum at $z^+_{rel} = 14$ near the rotating disk and at $z^+_{rel} = 13$ near the stationary disk. The other intensities, except $u'_r$ near the rotor, increase monotonically from the wall to an almost constant value away from the disks; $u'_r$ near the rotor has a maximum at $z^+_{rel} \approx 40$. The primary shear stress $\overline{u'_\theta u'_z}$ attains maxima at $z^+_{rel} = 29$ near the rotor and $z^+_{rel} = 31$ near the stator. In 2DTBLs the equivalent to the shear stress $\overline{u'_r u'_z}$ is zero. Near the disks, this stress component has a negative dip due to the change of sign of $\partial U_r/\partial z$. The third shear stress $\overline{u'_\theta u'_r}$ is usually neglected in the boundary layer equations where $\overline{u'_\theta u'_r}$ is differentiated only with respect to $\theta$ and $r$, i.e. in directions with no or only modest variation of statistical quantities. The wall-normal derivative of $\overline{u'_\theta u'_z}$ is typically two orders of magnitude larger than the spanwise derivative of $\overline{u'_\theta u'_r}$ near the walls, thereby indicating that $\overline{u'_\theta u'_r}$ is of negligible importance.

To study structural effects arising from the three-dimensionality of the mean flow, comparisons are made with plane Couette flow which is the two-dimensional equiv-

† As pointed out by an anonymous reviewer, the peak value 1.7 of the measured $u^+_{\theta,rms}$ is remarkably low compared to conventional turbulent boundary layers.

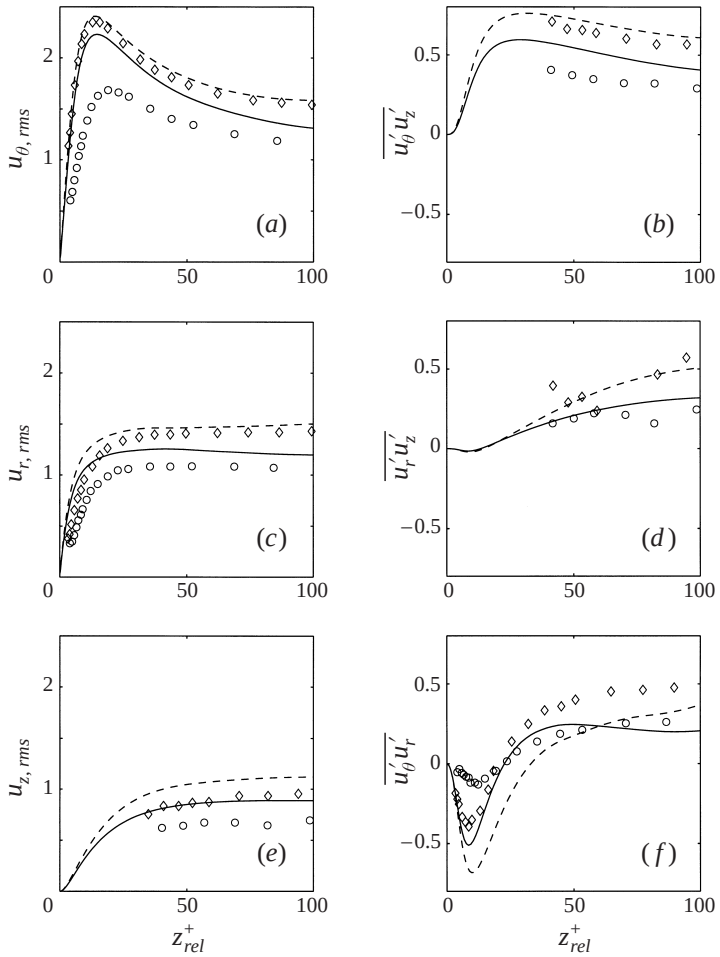


FIGURE 8. Reynolds stresses near the rotating disk (———, ○) and the stationary disk (— — —, ◇). Symbols are from Itoh (1995). Normalized with $u_\tau$.

alent of the rotor–stator flow. In Couette flow $\theta$, $r$ and $z$ represent the streamwise, spanwise and wall-normal directions, respectively. Figure 9 shows the anisotropy invariant map (AIM) for the Reynolds-stress tensor in the rotor–stator boundary layers and in the DNS of plane Couette flow by Bech *et al.* (1995). Following Lumley (1978) the invariants are

$$\mathrm{II} = \frac{1}{2}(a_{ii}a_{jj} - a_{ii}^2), \quad \mathrm{III} = \frac{1}{3!}(a_{ii}a_{jj}a_{kk} - 3a_{ii}a_{jj}^2 + 2a_{ii}^3), \tag{3.1}$$

where $a_{ij}$ is the anisotropy tensor of the second moments of the fluctuations:

$$a_{ij} = \overline{u_i' u_j'}/2k - \delta_{ij}/3. \tag{3.2}$$

$a_{ii}^2$ and $a_{ii}^3$ are the traces of $a_{ij}^2 = a_{ik}a_{kj}$ and $a_{ij}^3 = a_{ik}a_{kl}a_{lj}$, respectively. The data in the AIM are within the region limited by the two lines corresponding to axisymmetric flow and the straight upper line corresponding to the two-component limit. The one-dimensional state (outside the diagram) corresponds to large $-$II and III. Near the disks the wall-normal fluctuations are damped much more effectively than the

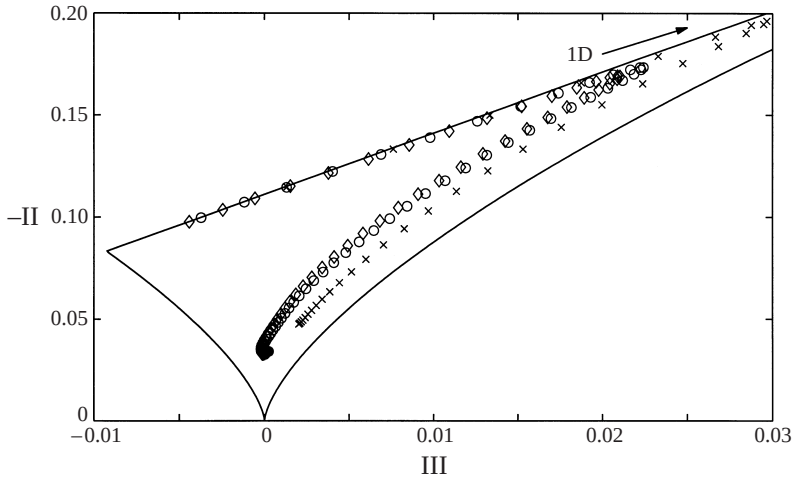


FIGURE 9. Anisotropy invariant map (AIM). Each symbol corresponds to a node in the computational grid. ○, Rotor side; ◇, stator side; ×, Couette flow from Bech *et al.* (1995).

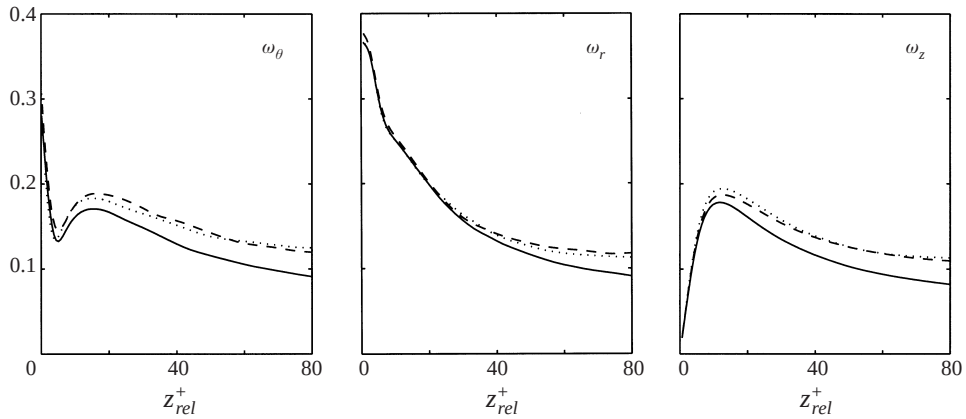


FIGURE 10. Root-mean-square vorticity fluctuations normalized by $\nu/u^2_{\theta\tau}$. ———, Rotor side; — — —, stator side; · · · · · ·, Couette flow data from Bech *et al.* (1995).

fluctuations parallel with the disks, as can be recognized from the points in the AIM that touch the two-component limit. Fluctuations midway between the disks are fairly close to the origin of the AIM, which corresponds to isotropic turbulence.

The anisotropy of the fluctuations near the two disks is quite similar. Compared to the disk flow the Couette flow is locally closer to the one-dimensional state. The streamwise fluctuations in the Couette flow are therefore relatively more significant than $u'_\theta$ in the disk flow. In addition the AIM reveals that the disk flow is shifted away from the axisymmetric state compared to the plane Couette flow. The disk flow is also closer to isotropy in the AIM. This could be partly due to the somewhat lower Reynolds number $Re_\tau$ in the Couette flow.

The profiles of the root-mean-square vorticity fluctuations are presented in figure 10. The vorticity fluctuations computed by Bech *et al.* (1995) are also plotted for comparison. Close to the wall the variation of the three vorticity components is almost the same near the rotor and the stator and in the Couette flow. Further out

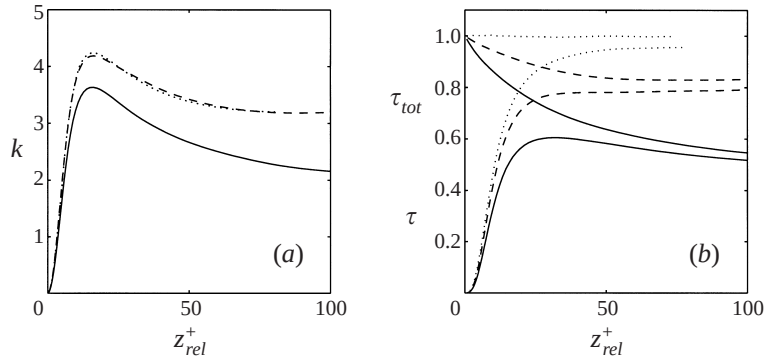


FIGURE 11. (*a*) Turbulent kinetic energy normalized with $u_{\theta\tau}$. (*b*) Magnitude of the turbulent shear stress vector $\tau$ and magnitude of the total shear stress $\tau_{tot}$. Normalized with $u_\tau$. Note that $\tau = 0$ and $\tau_{tot} = 1$ at $z^+_{rel} = 0$. Legend as in figure 10.

a surprisingly close agreement between the vorticity fluctuations near the stationary disk and in the Couette flow is observed. The level of the vorticity components near the rotating disk is lower than near the stationary disk, as could be expected from the levels of the Reynolds stresses in figure 8. Unlike turbulent velocity fluctuations, the root-mean-square vorticity fluctuations are approximately independent of the structure of the mean flow. In fact, for high Reynolds numbers the budget of the turbulent vorticity $\overline{\omega_i'\omega_i'}$ is approximately (see e.g. Tennekes & Lumley 1972)

$$\overline{\omega_i'\omega_j's_{ij}'} = \nu\overline{\frac{\partial\omega_i'}{\partial x_j}\frac{\partial\omega_i'}{\partial x_j}} \tag{3.3}$$

where $s_{ij}'$ is the strain rate fluctuations. This is probably the reason why the close agreement between the individual vorticity components near the stationary disk and in the Couette flow is not disrupted by the mean-flow three-dimensionality.

Figure 11(*a*) shows the turbulent kinetic energy $k$ from the present simulation and in the plane Couette flow simulation by Bech *et al.* (1995). The tangential friction velocity $u_{\theta\tau}$ in table 1 is used for the normalization of the rotor–stator flow. There is a remarkable similarity between the $k$-profile on the stator side and in the Couette flow. However by comparing the individual turbulence intensities this similarity is lost, in contrast to the individual vorticity components displayed in figure 10. The reason for this is naturally that the mean velocity field plays an essential role in the production of the velocity fluctuations.

The magnitude $\tau$ of the shear stress vector in planes parallel with the disks is shown in figure 11(*b*). For the disk flow $\tau = (\overline{u_\theta'u_z'}^2 + \overline{u_r'u_z'}^2)^{1/2}$, while for the Couette flow $\tau$ equals the only non-zero shear stress; $\tau$ exhibits a maximum about $z^+_{rel} \approx 30$ at the rotor side, whereas $\tau$ increases monotonically from the wall to a constant level on the stator side and in the Couette flow. For the disk boundary layers $\tau$ is substantially reduced compared to the Couette flow. In figure 11(*b*) the magnitude $\tau_{tot}$ of the total shear stress vector $(\nu\partial U_\theta/\partial z - \overline{u_\theta'u_z'}, \partial U_r/\partial z - \overline{u_r'u_z'})$ is also presented. The components refer to the tangential and radial directions, respectively. For the Couette flow the Reynolds-averaged Navier–Stokes equations can be integrated to give a constant total shear stress $\tau_{tot} = \nu\partial U/\partial y - \overline{u'v'} = u_\tau^2$. The magnitude of the total shear stress in the rotor–stator flow is reduced below this constant level. The non-zero radial mean velocity component leads to non-zero advection terms in the

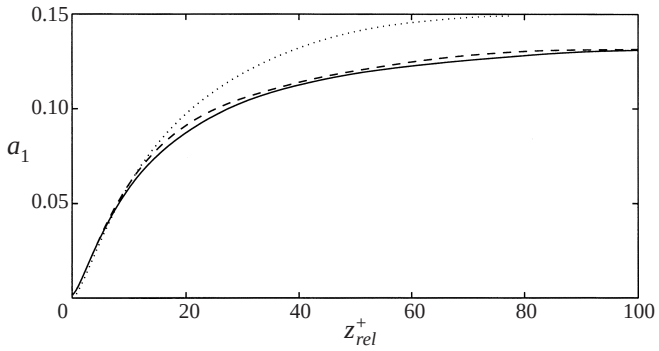


FIGURE 12. Structural parameter $a_1 = \tau/2k$. Legend as in figure 10.

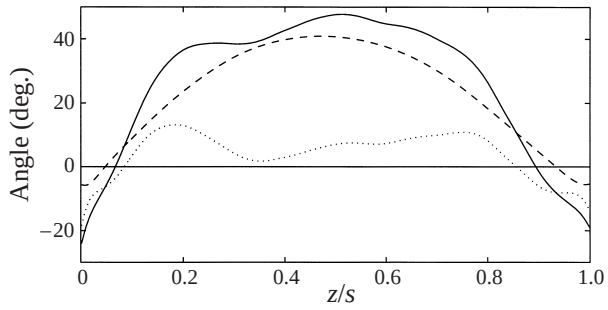


FIGURE 13. Mean gradient angle $\gamma_g$ (———), shear stress angle $\gamma_\tau$ (— — —) and the difference $\gamma_g - \gamma_\tau$ (· · · · · ·). (Further sampling would probably tend to increase the smoothness of the solid line.)

averaged Navier–Stokes equations, which in turn reduce the level of the total shear stress away from the walls. The structural parameter $a_1 = \tau/2k$ in figure 12 shows the relative significance of $\tau$. Typically $a_1 = 0.15$ in a wide range of two-dimensional turbulent boundary layers. For the Couette flow the structural parameter reaches 0.15 at $y^+ \approx 70$. For the three-dimensional boundary layers $a_1$ is reduced compared to the Couette flow and reaches a maximum of approximately 0.13 at $y^+ \approx 100$. This reduction of $a_1$ indicates that the turbulence in the rotor–stator flow is less efficient in extracting turbulence energy from the mean flow field. In addition, turbulence models which implicitly or explicitly assume that $a_1 = 0.15$ will inevitably tend to fail when applied to this flow.

Another feature of three-dimensional turbulent boundary layers is that the direction of the shear stress vector in planes parallel with the wall is not generally aligned with the mean velocity gradient vector. In cylindrical coordinates these vectors are $(\overline{u'_\theta u'_z}, \overline{u'_r u'_z})$ and $(\partial U_\theta/\partial z, \partial U_r/\partial z)$ where the components are in the tangential and radial direction. Turbulence models which rely on the assumption of an isotropic eddy viscosity will face problems when the misalignment between these vectors is large. In figure 13 the shear stress angle $\gamma_\tau = \arctan[\overline{u'_r u'_z}/\overline{u'_\theta u'_z}]$ and the mean gradient angle $\gamma_g = \arctan[(\partial U_r/\partial z)/(\partial U_\theta/\partial z)]$ are shown; $\gamma_\tau$ and $\gamma_g$ are the angles which $(\overline{u'_\theta u'_z}, \overline{u'_r u'_z})$ and $(\partial U_\theta/\partial z, \partial U_r/\partial z)$ make with the unit vector in the tangential direction. In non-stationary 3DTBLs the lag between $\gamma_g$ and $\gamma_\tau$ can be quite large (more than 50° in e.g. Coleman *et al.* 2000 and Le 1999). In stationary boundary layers the difference between $\gamma_g$ and $\gamma_\tau$ is generally smaller. Near the disks $\gamma_g$ is smaller than $\gamma_\tau$, while the situation is reversed further out. The greatest difference between $\gamma_g$ and $\gamma_\tau$ is 18° in

the present study. The errors which may arise from an assumption of eddy-viscosity isotropy could therefore be tolerable, at least from an engineering point of view.

### 3.3. *Reynolds stress transport*

The Reynolds stress transport equations can be written in tensorial form as

$$\frac{\mathrm{D}\overline{u_i'u_j'}}{\mathrm{D}t} = P_{ij} + D_{ij}^t + D_{ij}^v + \Pi_{ij} - \epsilon_{ij},$$

where

$$P_{ij} = -(\overline{u_i'u_k'}\partial U_j/\partial x_k + \overline{u_j'u_k'}\partial U_i/\partial x_k) \quad \text{(production)},$$

$$D_{ij}^t = -\partial\overline{u_i'u_j'u_k'}/\partial x_k \quad \text{(diffusion due to turbulent transport)},$$

$$D_{ij}^v = \nu\partial^2\overline{u_i'u_j'}/\partial x_k\partial x_k \quad \text{(viscous diffusion)},$$

$$\Pi_{ij} = \overline{u_i'\partial p'/\partial x_j} + \overline{u_j'\partial p'/\partial x_i} \quad \text{(velocity–pressure-gradient correlation)},$$

$$\epsilon_{ij} = -2\nu\overline{\partial u_i'/\partial x_k\partial u_j'/\partial x_i} \quad \text{(dissipation)}.$$

The transport equations in cylindrical coordinates can be found in e.g. Littell & Eaton (1991). The budgets for the turbulent kinetic energy $k$ and the magnitude of the shear stress vector $\tau$ are shown in figure 14. Here, the budgets for the plane Couette flow from the simulation by Bech *et al.* (1995) have also been included. The transport equation for $\tau$ is found through the relation

$$\frac{\mathrm{D}\tau}{\mathrm{D}t} = \frac{1}{\tau}\left(\overline{u_\theta'u_z'}\frac{\mathrm{D}\overline{u_\theta'u_z'}}{\mathrm{D}t} + \overline{u_r'u_z'}\frac{\mathrm{D}\overline{u_r'u_z'}}{\mathrm{D}t}\right).$$

The production term in the transport equation for $\tau$ is therefore defined as $P_\tau = (1/\tau)(\overline{u_\theta'u_z'}P_{\theta z} + \overline{u_r'u_z'}P_{rz})$ and likewise for the other terms.

Figure 14(*a*) shows that the terms in the transport equation for $k$ behave quite similarly in the rotor–stator flow and in the Couette flow. This is particularly the case for the stator boundary layer and the Couette flow, which had almost identical kinetic energy profiles (see figure 11). The peak in the production of turbulent energy is at approximately 11 wall units from the wall for all the profiles.

Since figure 11 reveals that the cause of the reduced parameter $a_1$ is a reduction in the shear stress vector, it should be possible to observe the reason for this reduction in the transport equation for $\tau$. But according to figure 14(*b*), this is not the case. Since $\tau$ is lower in boundary layers near the disks than near the plates in the Couette flow one would expect that in particular the production and dissipation terms would reflect this. However, $P_\tau$ is higher near the stationary disk than in the Couette flow at $z_{rel}^+ \gtrsim 10$ and the dissipation is stronger when $z_{rel}^+ \gtrsim 18$. The excess production of $\tau$ near the stator is mainly balanced by the diffusion due to turbulent transport. The differences between the rotating disk and the Couette flow is also smaller than what could be expected from figure 11(*b*). These budgets do therefore not reveal the cause of the reduced level of the shear stress near the disks.

## 4. Coherent structures

In order to try to understand the role played by the mean-flow three-dimensionality in the reduction of the magnitude of the shear stress vector, the focus of attention is now on the coherent vortical structures in the near-wall region. Previously,

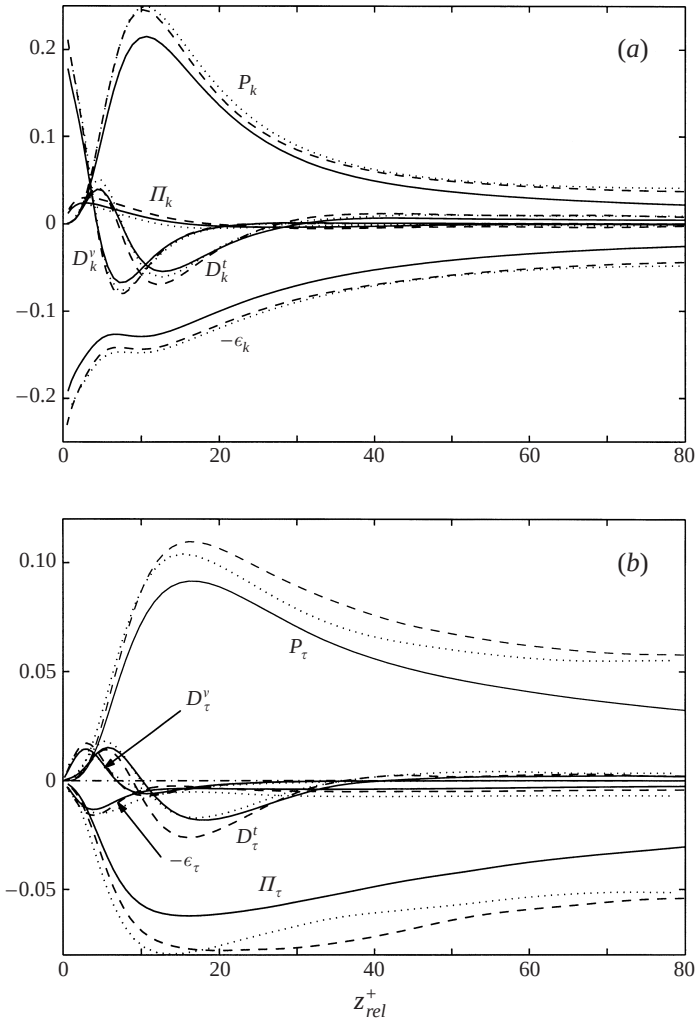


FIGURE 14. Budgets for (*a*) $k$ and (*b*) $\tau$. Normalized by $u_{\theta\tau}^4/\nu$. Legend as in figure 10.

conditional sampling techniques have been used in studying coherent structures in three-dimensional boundary layers. Littell & Eaton (1994), Kang *et al.* (1998), Le *et al.* (1999) and Wu & Squires (2000) conditioned on strong ejections and sweeps to extract information on modifications of coherent structures caused by the three-dimensionality. When triggering on velocity or stress signals, conditional averaging will always tend to smear out the averaged structures. With the objective to reduce this smearing effect, coherent structures are here obtained by ensemble averaging instantaneous vortices identified by the vortex definition suggested by Jeong & Hussain (1995). They defined a vortex as a connected region of negative $\lambda_2$, which is the second largest eigenvalue of the tensor $s_{ik}s_{kj} + r_{ik}r_{kj}$ where $s_{ij} \equiv (u_{i,j} + u_{j,i})/2$ is the strain rate and $r_{ij} \equiv (u_{i,j} - u_{j,i})/2$ is the rotation tensor. This vortex definition essentially captures localized pressure minima in the plane normal to the vortex axis. Jeong *et al.* (1997) showed that this vortex definition works satisfactorily in a turbulent channel flow. In the present investigation structures in the near-wall region, i.e. $z^+_{rel} < 50$, are in focus. As described in the introduction, the structures in this region in two-dimensional

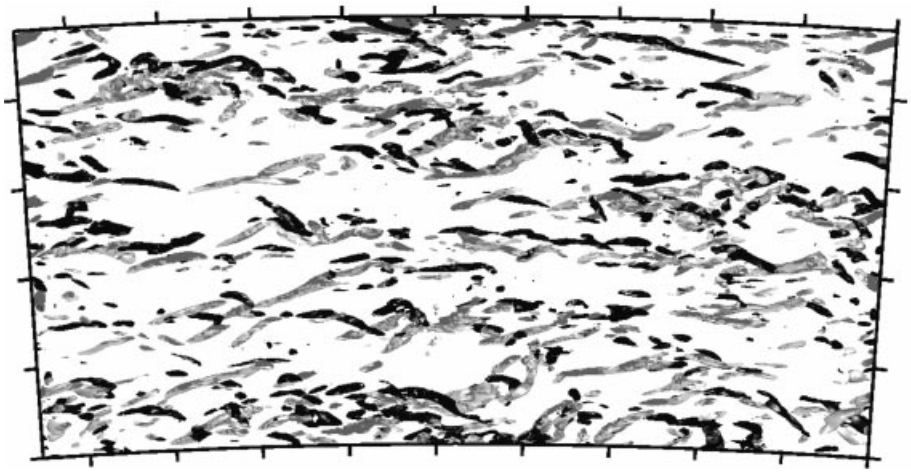

FIGURE 15. Isosurface plot (top view) of $\lambda_2 = -0.02$ in the region $0 < z^+_{rel} < 50$ near the rotating disk. Light (dark) shading represents Case 1 (Case 2). Tickmarks are 200 wall units apart. The tangential mean velocity in the rotating coordinate system is from left to right.

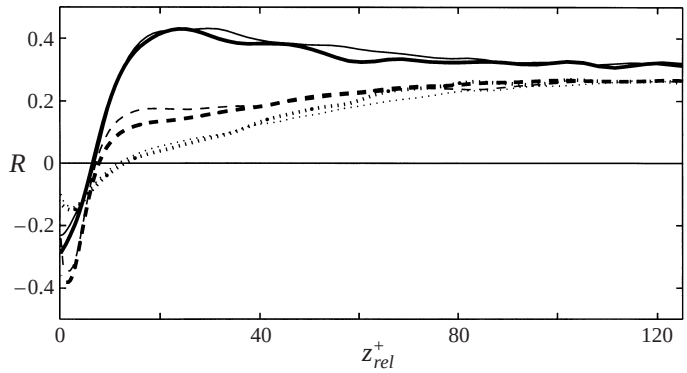


FIGURE 16. Cross-correlation of $-\lambda_2$ and ——, $|\omega'_\theta|$; · · · · · ·, $|\omega'_r|$; — — —, $|\omega'_z|$. Thin lines are near the rotor, thick lines near the stator.

flows are highly elongated vortices in the streamwise direction which are creating high- and low-speed streaks. Littell & Eaton (1994) hyphothesized that the coherent structures in their 3DTBL over a rotating disk were similar to the structures found in 2DTBLs. Wu & Squires (2000) compared different two-point spatial correlations deduced from their large-eddy simulation of rotating disk flow with measurements in 2DTBLs and concluded that there were indeed structural similarities between the two types of flows.

Figure 15 shows the isosurface $\lambda_2 = -0.02$ near the rotating disk. Light and dark shading represents Case 1 and Case 2 vortices, respectively, distinguished by the sign of the tangential vorticity, cf. figure 1. This isosurface plot shows elongated structures nearly aligned in the tangential direction, having a typical length of about 200 wall units. Case 1 vortices tend to tilt outwards, while Case 2 vortices are more aligned in the tangential direction. This significant difference in the degree of alignment of Case 1 and Case 2 vortices is obviously an effect of the crossflow.

The normalized cross-correlations between $-\lambda_2$ (since the vortex is associated with negative $\lambda_2$) and the magnitude of each of the components of the vorticity fluctuations

are shown in figure 16. In the near wall-region $10 < z^+_{rel} < 50$ the correlation between $-\lambda_2$ and $|\omega'_\theta|$ is significantly higher than between $-\lambda_2$ and the other two vorticity components. These cross-correlations therefore support the conclusion drawn from the instantaneous flow field visualized in figure 15, namely that the structures are aligned in the streamwise direction. Even closer to the disks ($z^+_{rel} < 10$) these correlations become strongly negative, probably due to the high vorticity near the walls caused by the no-slip condition. When the distance from the disks is large ($z^+_{rel} > 50$), the differences between the three cross-correlations are substantially reduced.

Motivated by the instantaneous vortex structures displayed in figure 15 and the cross-correlations in figure 16, elongated vortical structures nearly aligned in the tangential direction are further explored. After detection the detected structures are ensemble averaged. The detection and averaging are based on the scheme which Jeong *et al.* (1997) applied in identifying coherent structures in the near-wall region in turbulent channel flow. This procedure consists of three steps: (I) Detection of vortical structures by the $\lambda_2$-definition. The sign of the vortex is given by the streamwise component of the vorticity. (II) Ensemble-averaging structures of the same sign of rotation by aligning the mid-point of their streamwise length. The structures are required to have a streamwise length of at least 130 wall units in the region $10 < z^+_{rel} < 40$. (III) Shifting of the alignment point to maximize the cross-correlation between the individual structures and the ensemble-averaged field.

The total number of identified vortices of both signs of rotation, independent of tangential length, is found to be roughly equal. However, the number of Case 1 vortices of large tangential extent exceeds the number of long Case 2 vortices. This difference is more pronounced near the rotating disk than at the stationary disk. Therefore the numbers of Case 1 and Case 2 vortices included in the respective ensemble averages are not equal. Near the rotating disk the ensemble compromised 179 Case 1 and 101 Case 2 instantaneous structures. The corresponding numbers at the stator side are 68 and 60. The difference in the total numbers of identified vortices near the rotor and the stator is mainly due to the different $Re_\tau$ at the two disks, cf. table 1. The relative importance of the ensemble-averaged coherent structures can be seen by considering the fraction of the total examined area covered by the coherent structures. This fraction, defined as (total number of accepted vortices) $\times$ (area of projection of coherent structure into the $r,\theta$-plane)/(total examined $r,\theta$-area), turns out to be approximately 0.15 near both the rotor and the stator. The ensemble-averaged structures can therefore be considered as an important feature of the near-wall regions at the rotating and the stationary disks.

In the following presentation the origin $(\Delta r, \Delta\theta) = (0,0)$ in the plane parallel to the disks is defined to be the alignment point. The ensemble average is based on a database consisting of 12 instantaneous flow fields. The individual flow fields were separated in time by 71 and 46 inner time units ($\nu/u^2_{\theta\tau}$) near the rotor and stator sides, respectively. All variables are expressed in wall units.

### 4.1. *Structures on the rotor side*

To facilitate comparisons with conventional boundary layers, in which the streamwise mean velocity increases monotonically with the wall distance, the tangential velocity in this section is referenced to a coordinate system attached to the rotating disk. Isosurface plots of $\lambda_2(\langle u_i \rangle)$ for the educed coherent structures with negative $\omega_\theta$ (Case 1) and positive $\omega_\theta$ (Case 2) are presented in figure 17. The brackets $\langle\ \rangle$ indicate ensemble-averaged quantities, and the argument $\langle u_i \rangle$ means that $\lambda_2$ is calculated from the averaged field. The coherent structures in Jeong *et al.* (1997) had an inclination

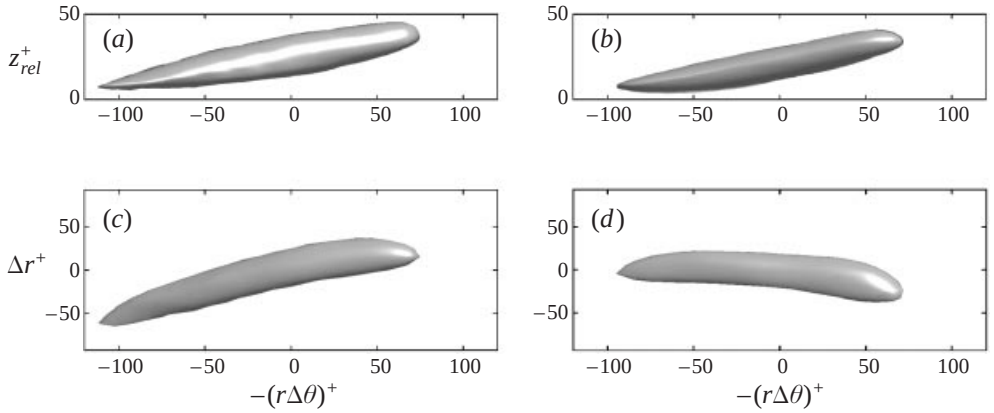


FIGURE 17. Isosurface plots of ensemble-averaged coherent structures near the rotating disk. (*a*) and (*c*) Side and top view of Case 1 coherent vortex. (*b*) and (*d*) Side and top view of Case 2 coherent vortex. In the rotating coordinate system the direction of the mean flow is to the right in these figures.

angle of about 9° in the vertical plane and tilting angles of $\pm 4°$ in the horizontal plane. Iwatsuki, Iida & Nagano (1999) also found similar inclination and tilting angles of the turbulence structures in a homogeneous shear flow. In the boundary layer near the rotating disk the coherent vortices of both signs have an inclination angle of approximately 10°. The tilting angle in the horizontal plane is about +15° for the Case 1 vortex and −3° for Case 2. The difference in tilting angles is likely to be a combined effect of the vertical inclination and the radial crossflow. The radial mean velocity exhibited a maximum at about $z^+_{rel} \approx 20$ in figure 6(*b*). The impact of the crossflow on the part of the vortices in the immediate vicinity of the disk is therefore weaker than further away from the disk, thereby explaining why the tilting angles increase in the positive direction.

In order to examine the interaction and spatial relation between coherent vortices of opposite sign, Jeong *et al.* (1997) performed an ensemble averaging with the alignment point located near the upstream end of the structures. Their motivation for this was that by aligning the structures at the mid-point, the ends are smeared out. An ensemble average of the structures near the rotating disk aligned at the upstream end of the structures left almost no trace of the oppositely signed vortex close to the alignment point. Compared with the findings of Jeong *et al.* (1997), the crossflow in the rotor–stator configuration seems to reduce the inter-vortical alignment found in 2DTBLs.

The coherent velocity fields in the $(r, z)$-plane through the alignment point are shown in figure 18. The thick solid lines are contours of $-\lambda_2$ indicating the position of the centre of the vortices. The velocities associated with Case 1 and Case 2 vortices exhibit similar patterns. The peak in positive $\langle u_\theta - U_\theta \rangle$ fluctuations is closer to the disk than the peak in negative fluctuations. This was also observed by Jeong *et al.* (1997) near the coherent structures in the two-dimensional boundary layer. However, in contrast to the observations by Jeong *et al.* (1997), the positive $\langle u_\theta - U_\theta \rangle$ fluctuations are quite strongly suppressed relative the negative fluctuations. This is especially the case for the Case 2 coherent vortex.

The radial fluctuations $\langle u_r - U_r \rangle$ directly reflect the radial velocity induced by the vortices. At the outboard side of the Case 1 vortex the radial fluctuation is negative due to transport in the positive $z$-direction of fluid having low radial mean velocity into regions with higher radial mean velocity.

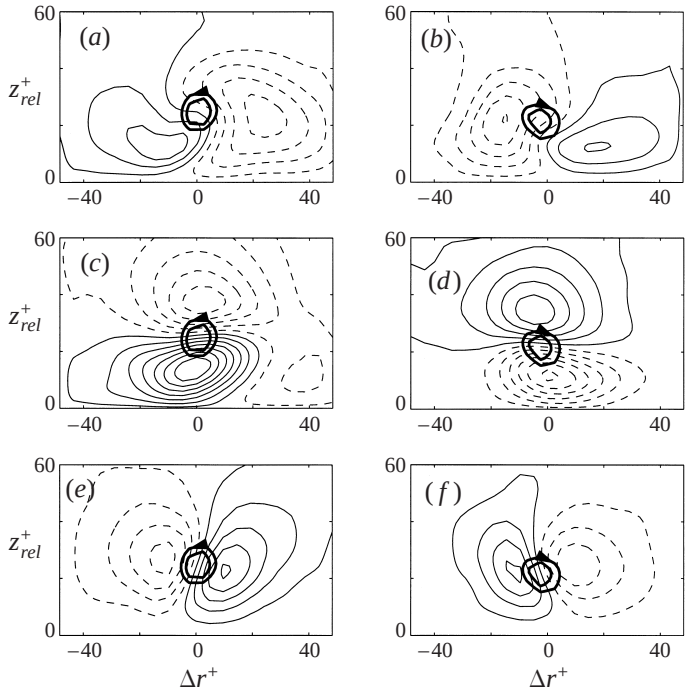


FIGURE 18. Ensemble-averaged coherent velocities near the rotating disk at $\Delta\theta = 0$. (*a*) and (*b*) $\langle u_\theta - U_\theta \rangle$, Case 1 and Case 2, contour increment 0.6; (*c*) and (*d*) $\langle u_r - U_r \rangle$, Case 1 and Case 2, contour increment 0.3; (*e*) and (*f*) $\langle u_z - U_z \rangle$ Case 1 and Case 2, contour increment 0.3. Dashed and solid lines represent negative and positive contours, respectively. Thick solid lines represent contours of $-\lambda_2$ and the arrow heads indicate the sense of rotation of the vortices.

Wall-normal velocity fluctuations $\langle u_z - U_z \rangle$ in figure 18(*e*, *f*) tend to be negative in the region where the circumferential fluctuations are positive and vice versa. At the centre of the vortices $\partial\langle u_z - U_z \rangle/\partial z$ is negative. The contour line $\langle u_z - U_z \rangle = 0$ is rotated in the opposite direction to the vortex rotation. The coherent vortices educed by Jeong *et al.* (1997) also showed this rotation of the zero-crossing of the wall-normal fluctuations, which was believed to be caused by the tilting of the coherent structure. Similar arguments hold here: due to the inclination of the vortices, $\langle u_\theta - U_\theta \rangle$ is negative upstream and positive downstream of the centre of both kind of vortices. Thus, in the non-rotating coordinate system $\partial\langle u_\theta \rangle/\partial\theta > 0$. The term $(1/r)\partial r\langle u_r \rangle/\partial r$ in the continuity equation is of marginal importance and therefore $\partial\langle u_z - U_z \rangle/\partial z < 0$ near the vortex centres.

Coherent Reynolds stresses are shown in figure 19. As seen from the rotating coordinate system, an ejection, defined as fluid moving out from the wall, is a Q2 (quadrant 2, $u_\theta < 0, u_z > 0$) event. Correspondingly, a sweep, defined as inward-moving fluid, is a Q4 event ($u_\theta > 0, u_z < 0$). The contours of the primary shear stress $-\langle u_\theta - U_\theta \rangle \langle u_z - U_z \rangle$ in figure 19(*a*, *b*) show the locations of the four types of events. The most noticeable difference between the Reynolds stresses associated with the coherent vortices close to the rotating disk and the coherent Reynolds stresses found by Jeong *et al.* (1997) is the reduction in the contribution from Q4 events to the shear stress $-\langle u_\theta - U_\theta \rangle \langle u_z - U_z \rangle$. While the contributions from Q2 and Q4 events to the primary shear stress were approximately equal in the 2DTBL, the contribution from Q4 events is only about 50% of the Q2 contribution near the Case 1 vortex and not

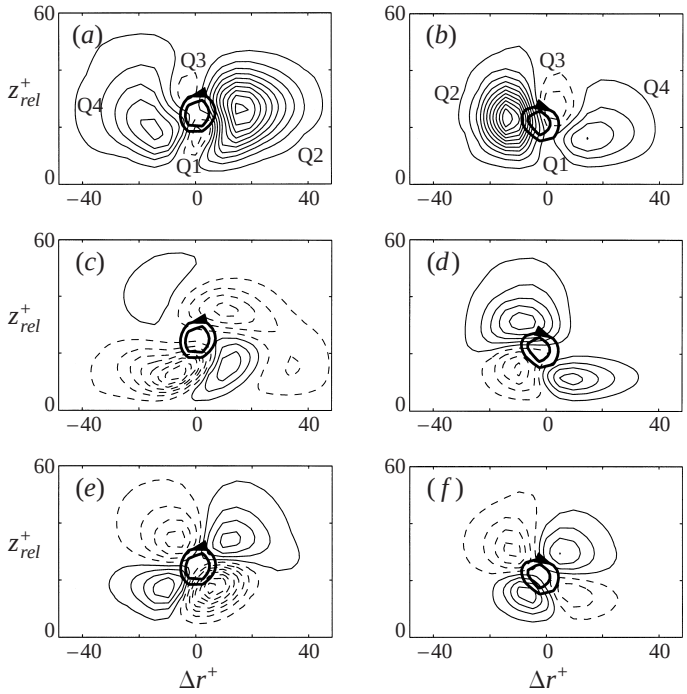


FIGURE 19. Ensemble-averaged coherent Reynolds stresses near the rotating disk at $\Delta\theta = 0$. Positive and negative contours are represented by solid and broken lines respectively. (*a*) and (*b*) $-\langle u_\theta - U_\theta\rangle\langle u_z - U_z\rangle$, Case 1 and Case 2, contour increment 0.25; (*c*) and (*d*) $-\langle u_\theta - U_\theta\rangle\langle u_r - U_r\rangle$, Case 1 and Case 2, contour increment 0.5; (*e*) and (*f*) $-\langle u_r - U_r\rangle\langle u_z - U_z\rangle$, Case 1 and Case 2, contour increment 0.25.

more than 30% of the Q2 contribution near the Case 2 vortex. Since the regions of negative $\langle u_z - U_z\rangle$ in figure 18(*e*, *f*) do not match the regions of positive $\langle u_\theta - U_\theta\rangle$ in figure 18(*a*, *b*), small regions of negative $-\langle u_\theta - U_\theta\rangle\langle u_z - U_z\rangle$ stress exist. These Q1 ($u_\theta > 0, u_z > 0$) and Q3 ($u_\theta < 0, u_z < 0$) events contribute only modestly to the Reynolds-averaged shear stress.

Contours of the shear stress $-\langle u_\theta - U_\theta\rangle\langle u_r - U_r\rangle$ are shown in figure 19(*c*, *d*). A positive contribution to the corresponding Reynolds stress from the coherent vortex of one sign was compensated by a negative contribution from the vortex of opposite sign in the study by Jeong *et al.* (1997). In the present flow, the distribution of positive and negative $-\langle u_\theta - U_\theta\rangle\langle u_r - U_r\rangle$ near the two vortices indicates that the net contribution from both vortices is positive near the rotating disk and negative away from the disk, i.e. in accordance with the result in figure 8(*f*).

The spatially averaged contribution to the stress $-\langle u_r - U_r\rangle\langle u_z - U_z\rangle$ from the individual coherent vortices is quite small due to the alternating pattern of positive and negative regions around each vortex, as can be seen in figure 19(*e*, *f*). It is difficult to see from these contour plots how the coherent vortices contribute to the small shear stress component $\overline{u_r' u_z'}$ in figure 8(*d*).

### 4.2. *Structures on the stator side*

In the presentation of flow structures near the stationary disk, $u_z$ is defined to be positive in the direction away from the disk. The radial velocity component is inverted, i.e. $u_r \to -u_r$, in order to make $u_r$ positive in the direction of the crossflow.

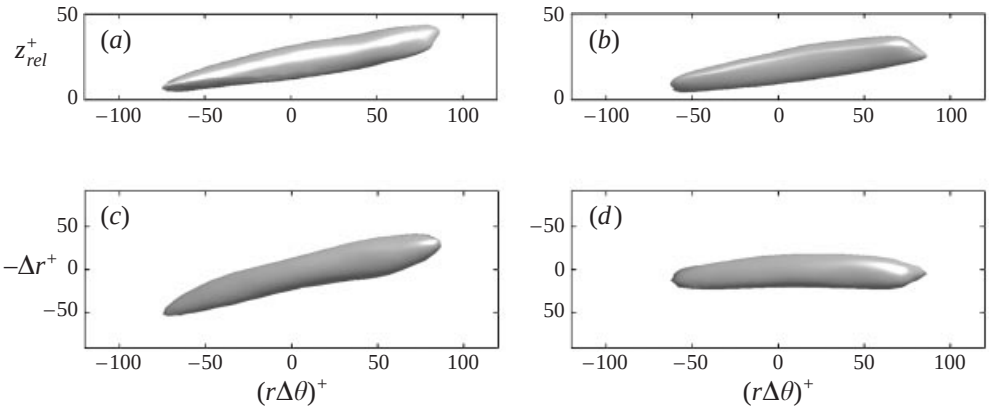


FIGURE 20. Isosurface plots of the ensemble-averaged coherent structures near the stationary disk. (*a*) and (*c*) Side and top view of Case 1 coherent vortex. (*b*) and (*d*) Side and top view of Case 2 coherent vortex.

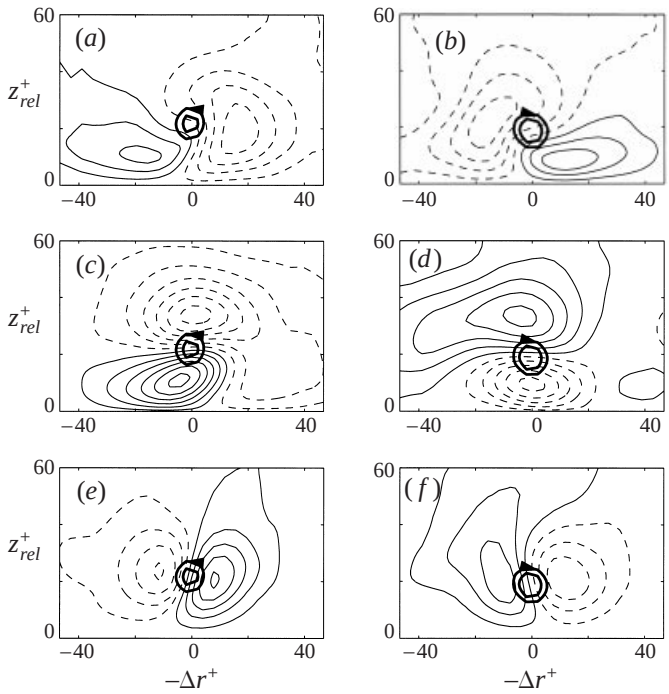


FIGURE 21. Ensemble-averaged coherent velocities near the stationary disk at $\Delta\theta = 0$: (*a*) and (*b*) $\langle u_\theta - U_\theta \rangle$ Case 1 and Case 2, contour increment 0.75; (*c*) and (*d*) $\langle u_r - U_r \rangle$ Case 1 and Case 2, contour increment 0.375; (*e*) and (*f*) $\langle u_z - U_z \rangle$ Case 1 and Case 2, contour increment 0.375.

These precautions facilitate comparisons of the coherent structures and accompanying velocities and stresses near the stator with the corresponding structures near the rotor side.

Isosurface plots of $\lambda_2(\langle u_i \rangle)$ are given in figure 20. As for the coherent structures near the rotating disk, the inclination angle in the vertical plane is about 10° for both kinds of vortices. The tilting angle in the horizontal plane is +15° for the Case 1 vortex and about 0° for Case 2.

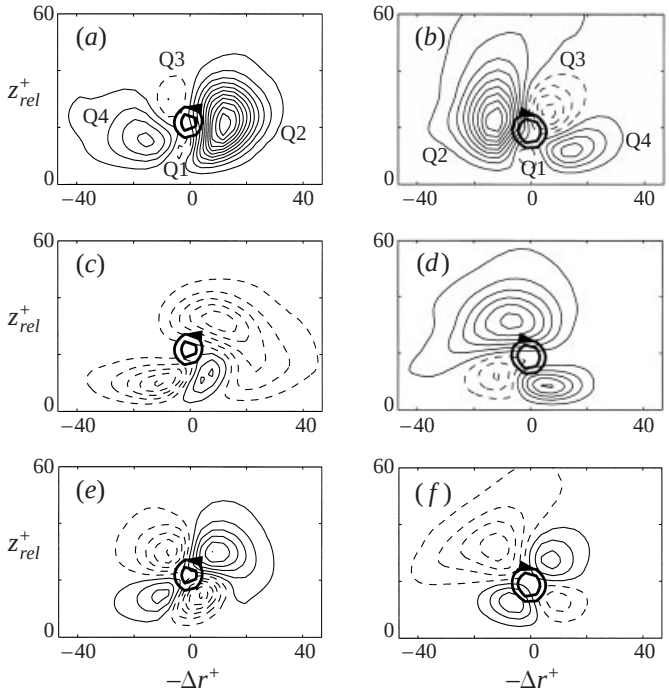


FIGURE 22. Coherent Reynolds stresses near the stationary disk at $\Delta\theta = 0$: (*a*) and (*b*) $-\langle u_\theta - U_\theta\rangle\langle u_z - U_z\rangle$ Case 1 and Case 2, contour increment 0.375; (*c*) and (*d*) $-\langle u_\theta - U_\theta\rangle\langle u_r - U_r\rangle$ Case 1 and Case 2, contour increment 0.75; (*e*) and (*f*) $-\langle u_r - U_r\rangle\langle u_z - U_z\rangle$ Case 1 and Case 2, contour increment 0.375.

An ensemble average with alignment point near the upstream end of the structures was also obtained near the stationary disk to gain insight into the amount of alignment between the vortices. Like for the structures near the rotating disk, the inter-vortical alignment is reduced as compared to that in two-dimensional flows.

It is interesting to see that the coherent velocities near the stationary disk (figure 21) show patterns that are quite similar to the coherent velocities near the rotating disk. Especially noteworthy is the observation that the region with positive $\langle u_\theta - U_\theta\rangle$ is substantially smaller in size and weaker in magnitude than the region of negative $\langle u_\theta - U_\theta\rangle$.

The similarity between the coherent velocities implies that the coherent Reynolds stresses in figure 22 are also similar to the stresses near the rotating disk. The contribution from Q4 events to the spatial averaged $-\langle u_\theta - U_\theta\rangle\langle u_z - U_z\rangle$-stress is small compared to the contribution from Q2 events, both for Case 1 and Case 2 coherent vortices.

### 4.3. *Conditional-averaged quadrant analysis*

In their study of the 3DTBL over a rotating disk Littell & Eaton (1994) measured conditionally-averaged velocities to gain insight into the near-wall coherent structures. Kang *et al.* (1998) performed a similar experiment on the rotating-disk boundary layer and examined the velocity fields near strong sweeps and ejections. By performing a quadrant analysis of the conditional-averaged fields they concluded that asymmetries in the radial direction observed by Littell & Eaton (1994) were caused by other events

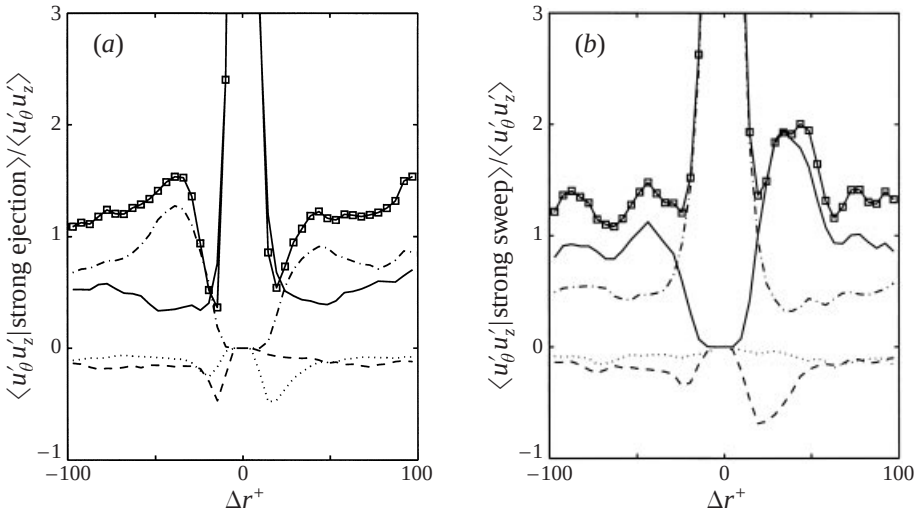


FIGURE 23. Conditional averages of $u'_\theta u'_z$ at $z^+_{rel} = 20$ near the rotor. (*a*) Strong ejections and (*b*) strong sweeps. —□—, Total. Contribution from – – –, Q1; ——, Q2; · · · · · ·, Q3; – · –, Q4.

than those related to coherent eddies, and that Case 1 and Case 2 vortices were symmetric like in two-dimensional boundary layers.

Here, quadrant analysis is applied to conditional-averaged shear stress near strong sweeps and ejections. The measurement locations of Littell & Eaton (1994) and Kang *et al.* (1998) were at $z^+ \simeq 115$ and $z^+ \simeq 90$, respectively, while the present detection point is at $z^+_{rel} = 20$. This choice is motivated by the cross-correlations in figure 16, which show that the structures in the rotor–stator flow lose their strong tendency to be aligned in the tangential direction at larger wall-normal distances, thus making the interpretation of the conditional averages more difficult. Here, a strong sweep is defined as $-u'_\theta u'_z > 3u'_{\theta,rms}u'_{z,rms}$ and $u'_z < 0$, while a strong ejection is detected when $-u'_\theta u'_z > 3u'_{\theta,rms}u'_{z,rms}$ and $u'_z > 0$.

The conditional averages near the rotor are given in figure 23. On each side of the primary peaks, caused by the strong sweeps and ejections, there is a smaller peak. Littell & Eaton (1994) interpreted these secondary peaks as traces of a pair of streamwise vortices generating the strong sweeps and ejections. Kang *et al.* (1998) refined this interpretation on the basis of their quadrant analysis and postulated that only positive shear-stress-producing events (Q2 and Q4) are signatures of streamwise vortices. On the left side of the central peak in figure 23(*a*) the secondary peak is associated with a Case 1 vortex and the secondary peak to the right is associated with a Case 2 vortex. The asymmetry in the total $-u'_\theta u'_z$ stress around $\Delta r = 0$ is mainly caused by Q4 events. Since the peak is highest on the left side, it can be concluded that Case 1 vortices are responsible for generating most of the strong ejections. Following the same line of argument, it is found that Case 1 vortices are also the primary source of generation of strong sweeps. Some further support for this conclusion is provided by Lygren & Andersson (2000).

The conclusion to be drawn from the conditional averages near the stationary disk in figure 24, is that Case 1 vortices contribute more to the Reynolds shear stress than Case 2 vortices. The total shear stress near an ejection is nearly symmetric. However, the quadrant analysis reveals that the peak from Q4 events is stronger on the left

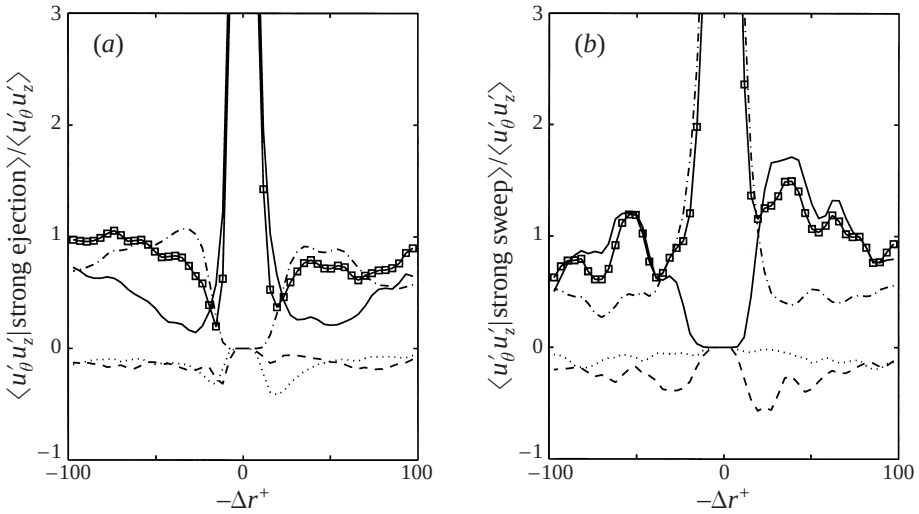


FIGURE 24. Conditional averages of $u'_\theta u'_z$ at $z^+_{rel} = 20$ near the stator. (*a*) Strong ejections and (*b*) strong sweeps. —□—, Total. Contribution from – – –, Q1; ——, Q2; · · · · · ·, Q3; – · –, Q4.

side of the primary peak, thereby implying that Case 1 vortices generate slightly more ejections than Case 2 vortices.

When the strength and spatial extent of the coherent stresses are taken into account, the observations from the conditional averages near both disks are in agreement with the coherent stresses in figures 19 and 22. The asymmetries in these conditional averages can also be explained by the difference in the numbers of large Case 1 and Case 2 vortices, as described in the introductory part of § 4.

## 5. Summary and concluding remarks

The flow in an angular section between a rotating and a stationary disk has been simulated numerically as an idealization of flows encountered in turbomachinery. Mean velocities and the turbulent stresses were compared to data from an experiment by Itoh (1995). The component intensities of the turbulence near the rotor were higher in this simulation than in the experiment. The reason for this is probably either that the present study concerned infinite disks while in the laboratory experiment the disks were enclosed by an outer shroud, or that the radial velocity component in the experiment transports fluid from the laminar region near the axis of rotation into the fully turbulent region further out. To rule out any Reynolds number effects a shorter simulation with $Re_{r_m} = 4.6 \times 10^5$ was performed. This simulation did not give significantly different results compared to the simulation at $Re_{r_m} = 4.0 \times 10^5$.

The wall friction at the rotating disk was substantially higher than on the stationary disk. It was moreover observed that in both the boundary layers near the rotor and near the stator, the shear stress vector and the mean flow gradient vector were more aligned than in non-stationary 3DTBLs. This modest misalignment indicates that closure models based on an isotropic eddy viscosity might have the potential to produce reliable results for this flow. The ratio of the shear stress vector magnitude to the turbulent kinetic energy was lower than the level usually observed in two-dimensional boundary layers. This reduction is commonly found in 3DTBLs, and has to be accounted for in turbulence models aimed at three-dimensional flow predictions.

Coherent structures in the three-dimensional boundary layers near the rotor and stator have been studied by means of ensemble averages of instantaneous vortices, and a conditional-averaged quadrant analysis. The instantaneous vortices included in the ensemble average were detected by the $\lambda_2$-criterion. Only structures with tangential extent exceeding 130 wall units were considered. An advantage of this detection scheme is that the smearing of the coherent structures is modest compared to sampling based on e.g. quadrant 2 and quadrant 4 detections.

The origin of the crossflow near the rotating disk is an imbalance between the centrifugal and pressure forces, while the crossflow near the stationary disk is pressure-driven. Nevertheless, the ensemble-averaged coherent structures in the boundary layers near the rotating and stationary disks were remarkably similar to each other. The observed differences between the present coherent structures and those found in 2DTBLs are therefore most likely caused solely by the three-dimensionality of the mean flow.

The coherent structures in the region considered ($z^+_{rel} < 50$) were highly elongated and nearly aligned in the streamwise direction. They were inclined 10° in the vertical plane. In the horizontal plane the Case 1 coherent vortex was tilted 15° while Case 2 vortices were more closely aligned with the tangential direction. The array of alternating-signed vortices overlapping in the streamwise direction, as found in the two-dimensional flow by Jeong *et al.* (1997), is broken by the crossflow. Another noticeable difference between the present coherent structures and the ones found by Jeong *et al.* (1997) is that the sweeps which are generated by the present vortices are much weaker than the ejections. This phenomenon can be associated with the 'stalls' and 'flip-overs' of vortices observed by Chiang & Eaton (1996) in their flow-visualization experiment. They found that the crossflow prevented some of the ejections caused by the vortices from rolling over and creating sweeps, thereby leading to stronger ejections and weaker sweeps.

Finally, a quadrant analysis of the conditional-sampled shear stress $-\overline{u'_\theta u'_z}$ around strong sweeps and ejections showed that the asymmetries which appeared were caused by Reynolds-stress-producing events. This supports the results by Littell & Eaton (1994) and is in contrast to conclusions arrived at by Kang *et al.* (1998). The in-depth exploration of the coherent structures in the rotor–stator flow suggests that the reason for the reduction of the structural parameter $a_1$ is the weakening of the stress production caused by the sweeps by the large-scale coherent structures of both signs of rotation.

This work has received support from The Research Council of Norway (Programme for Supercomputing) through a grant of computing time. ML was the recipient of a research fellowship offered by The Research Council of Norway under contract no. 115548/410. The authors gratefully acknowledge the valuable discussions with K. D. Squires (Arizona State University) and J. K. Eaton (Stanford University). M. Itoh (Nagoya Institute of Technology) provided us with his experimental data. The authors appreciate the considerable interest and valuable comments on the manuscript provided by the reviewers.

## REFERENCES

Anderson, S. D. & Eaton, J. K. 1989 Reynolds stress development in pressure-driven three-dimensional turbulent boundary layers. *J. Fluid Mech.* **202**, 263–294.

Andersson, H. I., Lygren, M. & Kristoffersen, R. 1998 Roll cells in turbulent plane Couette flow: Reality or artifact? In *16th Intl Conf. on Numerical Methods in Fluid Dynamics* (ed. C. H. Bruneau), pp. 117–122. Springer.

Batchelor, G. K. 1951 Note on a class of solutions of the Navier-Stokes equations representing steady rotationally-symmetric flow. *Q. J. Mech. Appl. Maths* **4**, 29–41.

Bech, K. H., Tillmark, N., Alfredsson, P. H. & Andersson, H. I. 1995 An investigation of turbulent plane Couette flow at low Reynolds numbers. *J. Fluid Mech.* **286**, 291–325.

Bradshaw, P. & Pontikos, N. S. 1985 Measurements in the turbulent boundary layer on an 'infinite' swept wing. *J. Fluid Mech.* **159**, 105–130.

Brady, J. F. & Durlofsky, L. 1987 On rotating disk flow. *J. Fluid Mech.* **175**, 363–394.

Cheah, S. C., Iacovides, H., Jackson, D. C., Ji, H. & Launder, B. E. 1994 Experimental investigation of enclosed rotor-stator disk flows. *Expl Thermal Fluid Sci.* **9**, 445–455.

Chiang, C. & Eaton, J. K. 1996 An experimental study of the effects of three-dimensionality on the near wall turbulence structures using flow visualization. *Exps Fluids* **20**, 266–272.

Coleman, G. N., Ferziger, J. H. & Spalart, P. R. 1990 A numerical study of the turbulent Ekman layer. *J. Fluid Mech.* **213**, 313–348.

Coleman, G. N., Kim, J. & Spalart, P. R. 1996 Direct numerical simulation of strained three-dimensional wall-bounded flows. *Expl Thermal Fluid Sci.* **13**, 239–251.

Coleman, G. N., Kim, J. & Spalart, P. R. 2000 A numerical study of strained three-dimensional wall-bounded turbulence. *J. Fluid Mech.* **416**, 75–116.

Cooper, P. & Reshotko, E. 1975 Turbulent flow between a rotating disk and a parallel wall. *AIAA J.* **13**, 573–578.

Daily, J. W. & Nece, R. E. 1960 Chamber dimension effects on induced flow and frictional resistance of enclosed rotating disks. *Trans. ASME J. Basic Engng* **82**, 217–232.

Eaton, J. K. 1995 Effects of mean flow three dimensionality on turbulent boundary-layer structure. *AIAA J.* **33**, 2020–2025.

Fanneløp, T. K. & Krogstad, P. Å. 1975 Three-dimensional turbulent boundary layers in external flows: a report on Euromech 60. *J. Fluid Mech.* **71**, 815–826.

Flack, K. A. 1997 Near-wall structure of three-dimensional turbulent boundary layers. *Exps Fluids* **23**, 335–340.

Itoh, M. 1995 Experiments on the turbulent flow in the narrow clearance between a rotating and a stationary disk. In *Turbulent Flows* (ed. B. F. Carroll, T. Kobayashi & M. J. Morris). ASME-FED, vol. 208, pp. 27–32.

Itoh, M., Yamada, Y., Imao, S. & Gonda, M. 1992 Experiments on turbulent flow due to an enclosed rotating disk. *Expl Thermal Fluid Sci.* **5**, 359–368.

Iwatsuki, M., Iida, O. & Nagano, Y. 1999 Turbulence structure and transport mechanism in a homogeneous shear flow (Reynolds number effects). In *Turbulence and Shear Flow Phenomena – 1* (ed. S. Banerjee & J. K. Eaton), pp. 481–486. Begell House.

Jeong, J. & Hussain, F. 1995 On the identification of a vortex. *J. Fluid Mech.* **285**, 69–94.

Jeong, J., Hussain, F., Schoppa, W. & Kim, J. 1997 Coherent structures near the wall in a turbulent channel flow. *J. Fluid Mech.* **332**, 185–214.

Johnston, J. P. & Flack, K. A. 1996 Review – advances in three dimensional turbulent boundary layers with emphasis on the wall-layer regions. *Trans. ASME J. Fluids Engng* **118**, 219–232.

Kang, H. S., Choi, H. C. & Yoo, J. Y. 1998 On the modification of the near-wall coherent structure in a three-dimensional turbulent boundary layer on a free rotating disk. *Phys. Fluids* **10**, 2315–2322.

Kármán, T. von 1921 Uber laminare und turbulente reibung. *Z. Angew. Math. Mech.* **1**, 233–252.

Kobayashi, R. 1994 Review: Laminar-to-turbulent transition of three-dimensional boundary layers on rotating bodies. *Trans. ASME J. Fluids Engng* **116**, 200–211.

Le, A.-T. 1999 A numerical study of three-dimensional turbulent boundary layers. PhD thesis, Department of Mechanical and Aerospace Engng, University of California, Los Angeles.

Le, A.-T., Coleman, G. N. & Kim, J. 1999 Near-wall turbulence structures in three-dimensional boundary layers. In *Turbulence and Shear Flow Phenomena – 1* (ed. S. Banerjee & J. K. Eaton), pp. 151–156. Begell House.

Littell, H. S. & Eaton, J. K. 1991 An experimental investigation of the three-dimensional boundary layer on a rotating disk. *Tech. Rep.* MD-60. Stanford University, Department of Mechanical Engineering, Thermosciences Div.

Littell, H. S. & Eaton, J. K. 1994 Turbulence characteristics of the boundary layer on a rotating disk. *J. Fluid Mech.* **266**, 175–207.

Lumley, J. L. 1978 Computational modeling of turbulent flows. *Adv. Appl. Mech.* **18**, 123–176.

LUND, T. S., WU, X. & SQUIRES, K. D. 1998 Generation of turbulent inflow data for spatially-developing boundary layer simulations. *J. Comput. Phys.* **140**, 233–258.

LYGREN, M. & ANDERSSON, H. I. 2000 Near-wall structures in turbulent rotor-stator flow. In *Advances in Turbulence VIII*. (ed. C. Dopazo), pp. 675–678. CIMNE.

MOIN, P., SHIH, T. H., DRIVER, D. & MANSOUR, N. N. 1990 Direct numerical simulation of a three-dimensional turbulent boundary layer. *Phys. Fluids* A **2**, 1846–1853.

OWEN, J. M. & ROGERS, R. H. 1989 *Flow and Heat Transfer in Rotating-Disc Systems, Volume 1 – Rotor–Stator Systems*. Resarch Studies Press, Taunton (John Wiley).

ROBINSON, S. K. 1991 Coherent motions in the turbulent boundary layer. *Ann. Rev. Fluid Mech.* **23**, 601–639.

SENDSTAD, O. & MOIN, P. 1991 On the mechanics of 3-D turbulent boundary layers. *Proc. 8th Symp. Turbulent Shear Flows, Munich, Germany, Sept. 9–11* pp. 5.4.1–5.4.5.

SHIZAWA, T. & EATON, J. K. 1992 Turbulence measurements for a longitudinal vortex interacting with a three-dimensional turbulent boundary layer. *AIAA J.* **30**, 49–55.

SPALART, P. R. 1988 Direct simulation of a turbulent boundary layer up to $Re_\theta = 1410$. *J. Fluid Mech.* **187**, 61–98.

SPALART, P. R. 1989 Theoretical and numerical study of a three-dimensional turbulent boundary layer. *J. Fluid Mech.* **205**, 319–340.

SPALART, P. R. & WATMUFF, J. H. 1993 Experimental and numerical study of a turbulent boundary layer with pressure gradients. *J. Fluid Mech.* **249**, 337–371.

STEWARTSON, K. 1953 On the flow between two rotating coaxial disks. *Proc. Camb. Phil. Soc.* **49**, 333–341.

TENNEKES, H. & LUMLEY, J. L. 1972 *A First Course in Turbulence*. The MIT Press.

WU, X. & SQUIRES, K. D. 1997 Large eddy simulation of an equilibrium three-dimensional turbulent boundary layer. *AIAA J.* **35**, 67–74.

WU, X. & SQUIRES, K. D. 1999 Large eddy simulation of the turbulent flow over a rotating disk. In *Turbulence and Shear Flow Phenomena – 1* (ed. S. Banerjee & J. K. Eaton), pp. 163–168. Begell House.

WU, X. & SQUIRES, K. D. 2000 Prediction and investigation of the turbulent flow over a rotating disk. *J. Fluid Mech.* **418**, 231–264.

ZANDBERGEN, P. J. & DIJKSTRA, D. 1987 Von Kármán swirling flows. *Ann. Rev. Fluid Mech.* **19**, 465–491.